UK Atomic Energy Authority

UKAEA-STEP-PR(22)01

B.S. Patel, D. Dickinson, C.M. Roach, H.R. Wilson

Linear gyrokinetic stability of a high beta non-inductive spherical tokamak

Enquiries about copyright and reproduction should in the first instance be addressed to the UKAEA Publications Officer, Culham Science Centre, Building K1/0/83 Abingdon, Oxfordshire, OX14 3DB, UK. The United Kingdom Atomic Energy Authority is the copyright holder.

The contents of this document and all other UKAEA Preprints, Reports and Conference Papers are available to view online free at scientific-publications.ukaea.uk/

Linear gyrokinetic stability of a high beta non-inductive spherical tokamak

B.S. Patel, D. Dickinson, C.M. Roach, H.R. Wilson

This is a preprint of a paper submitted for publication in
Nuclear Fusion

Linear gyrokinetic stability of a high β non-inductive spherical tokamak

B.S. Patel[1,2], D. Dickinson[1], C.M. Roach[2] and H.R. Wilson[1]

[1] University of York, Heslington, York, YO10 5DD, UK
[2] Culham Centre for Fusion Energy, Abingdon OX14 3DB, UK

E-mail: bhavin.s.patel@ukaea.uk

March 2021

Abstract. Spherical tokamaks (STs) have been shown to possess properties desirable for a fusion power plant such as achieving high plasma β and having increased vertical stability. To understand their confinement properties in a reactor relevant regime a $1GW$ fusion power spherical tokamak plasma equilibrium was analysed using linear gyrokinetics to determine the type of micro-instabilities that arise. Kinetic ballooning modes (KBMs) and micro-tearing modes (MTMs) are found to be the dominant instabilities. The parametric dependence of these linear modes was determined and from the insights gained, the equilibrium was optimised to find a regime marginally stable to all micro-instabilities. This work indicates the physics needed to perform transport modelling in high β ST regimes such as for STEP.

1. Introduction

Understanding the confinement of tokamak plasmas in reactor relevant regimes is critical in the design of future fusion power plants. Scaling laws, such as the ITER98 IPB(y,2) [1] and the Petty08 [2] are often used as a metric for the quality of confinement. Both of these laws describe the confinement of existing conventional tokamaks equally well but extrapolate quite differently to reactor relevant regimes. For example, for the ITER baseline scenario the 98 scaling predicts $\tau_{98} = 3.7s$, but Petty predicts an increased value of $\tau_{Petty} = 4.6s$. Furthermore, they have been based off of existing tokamak data, which would not account for additional physics relevant in burning plasma regimes. These metrics can be used for ballpark estimates in confinement, but in reality the confinement is largely set by neoclassical and turbulent transport and reliable predictions should be based on first principle models for these. Gyrokinetics has proven to be a useful tool in diagnosing the source of turbulence and has been able to match experimental fluxes with reasonable success [3–5]. Applying linear gyrokinetics to a high β ST regime will provide an insight into the modes that may arise. This work aims to identify the linear micro-stability of a $1GW$ fusion power ST plasma equilibrium and highlight the necessary

physics that needs to be captured in a transport model. This is especially critical for the design of ST reactor designs such as STEP.

In Section **??**, a non-inductive scenario is developed using SCENE [6], a fixed boundary Grad-Shafranov solver. Section 3, the dominant instabilities of a core flux surface was determined using linear GS2 illustrating the nature of the modes that need to captured in a transport model. Section 4 explores the impact of different equilibrium parameters on these modes. With the insights gained here, Section 5 examines different global plasma parameters that can be modified to achieve a more stable equilibrium. An equilibrium marginally to all the micro-instabilities is found and the feasibility of such an equilibrium is discussed. Appendix Appendix B discusses the explores the cause of stability in the electron scale region and Appendix Appendix A compares the predictions made by CGYRO and GS2 for this equilibrium showing them to be in good agreement.

2. $1GW$ Fusion power spherical tokamak scenario

This plasma equilibrium was designed with a fusion power over $1GW$ as this was assumed to be sufficient to provide net electricity. In SCENE several global plasma parameters are specified such the the current going through the central column (which sets the vacuum magnetic field), the total plasma current and the plasma boundary. Furthermore, the the temperature and density profiles are specified, though no transport models inform these profiles. The feasibility of the profiles could be tested by calculating the heat and particle sources required for a given transport model.

SCENE solves the equilibrium consistent with the neoclassical currents such as the bootstrap and diamagnetic current, returning the amount of auxiliary current needed to provide the total plasma current requested. The shape of auxiliary current profile is set by the user such that they can enforce the auxiliary current to driven on or off the magnetic axis.

A major radius of $2.5m$ was set and an aspect ratio of 1.67 allows sufficient space for the centre column to carry $I_{rod} = 30MA$, generating $2.4T$ on axis. A plasma current of $I_p = 21MA$ provides a $\beta_N = 5.5$, which satisfies MHD stability constraints with a given q profile. The elongation was set to $\kappa = 2.8$, inline with aspect ratio scalings from NSTX [7] and the triangularity of $\delta = 0.55$ is consistent with poloidal field coils. The pedestal was designed to be similar to ITER's where pedestal top occurs at $\rho_\psi = 0.9$ with a temperature height of $T_{ped} = 5keV$ [8]. A small amount of density peaking was specified such that $n_{e,ped}/n_{e0} = 0.9$. Using an "ITER-like" pedestal may not be valid in this regime as there is evidence that the pedestal width and height scales differently in STs [9] so this needs to be further examined with a pedestal model such as EPED, but is not expected to influence our results on the core plasma stability. The core temperature was set to $28keV$ with the $T_e = T_i$. The density was then scaled up such that $P_{fus} > 1GW$. These profiles are shown in Figure 1a. The resulting equilibrium is outlined in Table 1, with Figure 1b illustrating the flux surfaces.

The auxiliary current profile was set to be primarily off axis which reduced the

internal inductance l_i to help with vertical stability, with a small amount necessary on axis to fill the hole in the bootstrap current. From Table 1, it can be seen that $8.2MA$ of auxiliary current was necessary for a non-inductive scenario. Using NUBEAM [10] an NBI configuration was identified capable of driving the required current. For the on axis current, an $8MW$ $1MeV$ beam was necessary and $86MW$ $500keV$ for the off axis current.

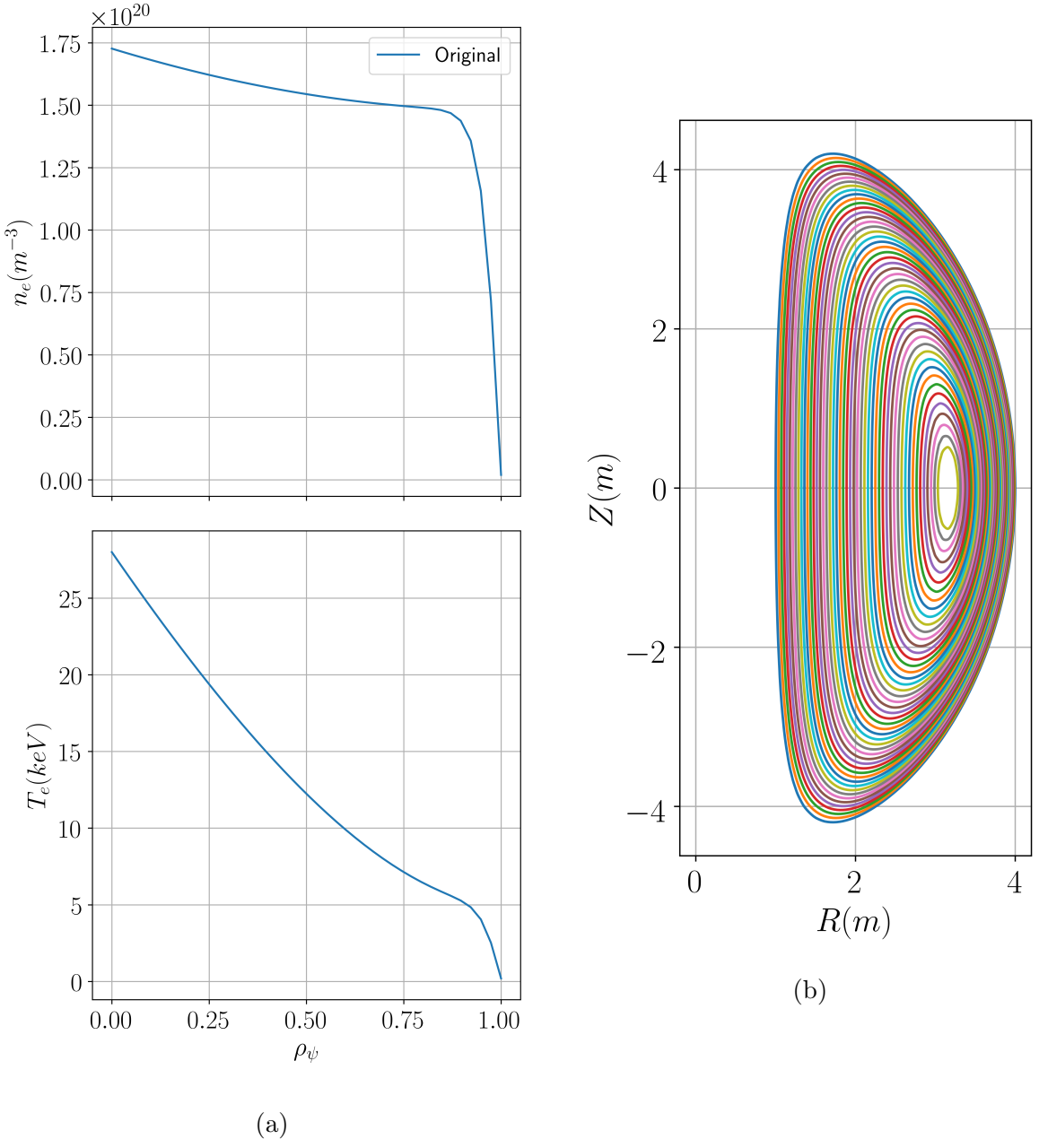

(a) (b)

Figure 1: a) Electron density and temperature profiles and b) flux surfaces of the baseline equilibrium.

To begin with the dominant instabilities will be examined on a core flux surface where $\rho_\psi =$

Parameter	Value	Motivation
R_{maj} (m)	2.5	Power loading to the wall
a (m)	1.5	Allow space for centre column
R_0 (m)	3.15	Magnetic axis position - output from SCENE
I_{rod} (MA)	30.0	MHD stability
I_p (MA)	21.0	Trade-off between confinement and current drive
I_{aux} (MA)	8.2	Output from SCENE
$P_{fus}(MW)$	1100	$P_{net} > 0$
$P_{aux}(MW)$	94	NUBEAM
κ	2.8	Limits based off of NSTX data
δ	0.55	PF coil configuration
H_{98}, H_{Petty}	1.35, 0.94	Confinement determined by Petty scaling law (output)
$T_{e0}, \langle T_e \rangle (keV)$	28.0, 14.8	Current drive efficiency
$n_{e0}, \langle n_e \rangle (\times 10^{20} m^{-3})$	1.72, 1.54	Ensure $P_{fus} = 1.1GW$ given T_e assumption
f_{GW}	0.54	Ensure $P_{fus} = 1.1GW$ given T_e assumption
l_i	0.27	Maximise elongation
β_N	5.5	Output from SCENE - MHD stable
q_0	2.51	Avoid sawteeth/NTM/internal kink modes

Table 1: Basic plasma parameters for this baseline scenario and the reasoning behind them.

$\psi/\psi_{LCFS} = 0.5$ with ψ_{LCFS} being the poloidal flux at the last closed flux surface. Once the nature of the modes is identified, the parametric dependence of these modes will be determined which, in turn, will inform design choices that will help stabilise the equilibrium. Two other flux surfaces at $\rho_\psi = 0.3$ and 0.7 were briefly examined to see if similar modes arise.

2.1. Equilibrium parameters

A Miller parameterisation [11] was used to model this equilibrium as it allows for easier cross-code validation, with the parameters outlined in Table 2. The fit of the flux surface and poloidal field are shown in Figures 3a and 3b respectively. The Miller fit and the equilibrium are in agreement. Simulations were conducted using the full numerical equilibrium and it was found to agree with the Miller simulations.

2.1.1. Numerical set-up Convergence tests in GS2 indicated that 128 θ points per poloidal revolution, 8 energy grid points and 16 un-trapped grid points in pitch angle‡ was sufficient to resolve the modes seen here. Two species were simulated, a thermal deuterium and electron species. The impact of including tritium, impurities and fast ions is left as future work. The normalisation used here was that from CGYRO [12] where $k_y = nq/r$ which is normalised to $\rho_s = \frac{c_s}{eB_{unit}/m_D c}$. Here $c_s = \sqrt{T_e/m_D}$ and $B_{unit} = q/r\partial\psi/\partial r$. This also leads to a different definition of normalised β where $\beta_{e,unit} = \frac{n_e T_e}{B^2_{unit}}$. It should be noted that this isn't the normalisation used in GS2, but was chosen to allow for easier comparison to CGYRO in appendix Appendix A.

‡ In GS2 the number of trapped grid points in pitch angle is given by $n_\theta/2 + 1$.

Parameter	$\rho_\psi = 0.3$	$\rho_\psi = 0.5$	$\rho_\psi = 0.85$
r/a	0.50	0.66	0.89
R_{maj}/a	1.88	1.79	1.66
n_{e20} (m^{-3})	1.60	1.51	1.44
$T_e(keV)$	17.8	12.2	5.8
a/L_n	0.26	0.43	0.56
a/L_T	1.86	2.77	3.50
Δ	-0.52	-0.57	-0.47
q	3.42	4.30	5.53
$\hat{s}$	0.69	0.78	1.22
κ	3.23	3.03	2.84
s_κ	-0.17	-0.14	-0.06
δ	0.40	0.45	0.47
s_δ	0.16	0.19	0.26
β_e	0.27	0.15	0.06
$\beta_{e,unit}$	0.023	0.012	0.0035
ρ^*	0.0019	0.0014	0.00075
$\nu_{ei}(c_s/a)$	0.0085	0.017	0.068
$\gamma_{dia}(c_s/a)$	0.04	0.08	0.12

Table 2: Plasma and Miller parameters for 3 flux surfaces, $\rho_\psi = 0.3, 0.5 \,\&\, 0.85$ for the equilibrium in Table 1.

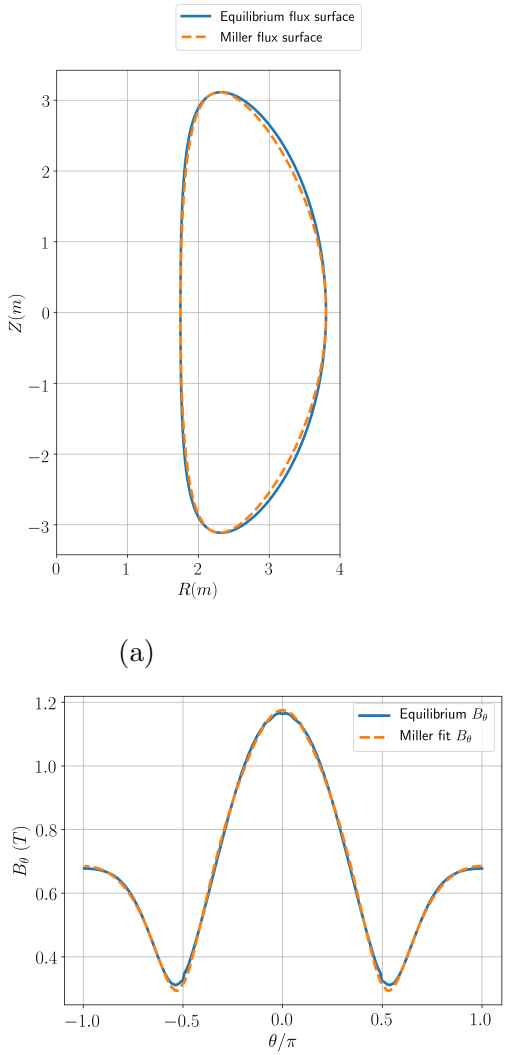

Figure 2: Miller fit shown for $\rho_\psi = 0.5$ surface showing the a) flux surface contour and b) the poloidal field

3. Identifying the important instabilities

3.1. Dominant instabilities

The prevailing instabilities of the $\rho_\psi = 0.5$ surface at an initial ballooning angle of $\theta_0 = 0$ are shown in Figure 3. Three different types of modes were found; in the very long wavelength region when $k_y < 0.6$, MTMs were found which will be illustrated by filled orange triangles. At slightly shorter wavelengths, but still at the ion scale where $0.1 < k_y < 2.0$, KBMs were found, denoted by hollow blue circles. Finally as the electron scale is approached between $3.0 < k_y < 6.0$, another MTM is found shown by filled magenta squares, though this will be shown to be different in nature to the low k_y MTMs. The figure markers for each type of mode will be kept consistent throughout this work, to easier allow for

identification of different modes. Furthermore, a hollow data point will correspond to an even parity ϕ eigenfunctions and a filled data point to an odd parity mode.

From Figure 3, it can be seen that dominant mode transitions from the MTMs to the KBMs, with the MTMs being subdominant above $k_y = 0.14$. Co-existing MTMs and KBMs have been seen before in simulations of JET, DIII-D, MAST and NSTX plasmas [13–17]. Nonlinear simulations will be necessary to determine their relative contributions to the total turbulent transport. Normally it would be necessary to have an eigensolver to resolve these modes, but in GS2 it is possible to enforce an odd or even ϕ eigenfunction. This allows for usage as a pseudo-eigensolver to determine the dominant odd or even eigenmode. It should be noted that an odd ϕ eigenfunction doesn't ensure the MTM is found, just that the mode found will have odd parity. The eigenfunctions of these modes are shown in Figure 4.

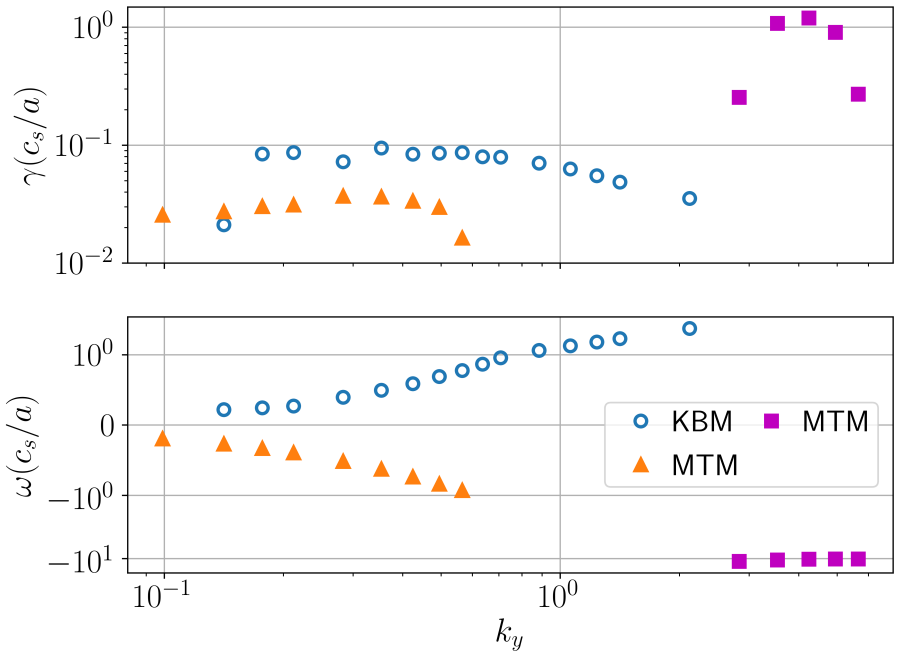

Figure 3: Eigenvalues of the instabilities for the $\rho_\psi = 0.5$ surface of the baseline equilibrium calculated by GS2. The hollow marker denotes an even parity eigenfunction and a filled marker an odd eigenfunction. Note the log scale.

In this work an MTM will refer to any electron direction mode that has field line tearing. MTMs are generally identified with an even parity $A_{||}$ eigenfunction which is symmetric about $\theta = 0$ (with ϕ being odd). However this does not guarantee tearing and a more precise definition can be used that quantifies this. A mode is tearing if the perturbation results in a field line that does not return to the equilibrium flux surface. This can be characterised using the following equation [18–20]

$$C_{tear} = \frac{|\int A_{||} dl|}{\int |A_{||}| dl} \tag{1}$$

which $\int dl$ corresponds to an integral along the field line. $C_{tear} = 1$ corresponds to a purely tearing mode and $C_{tear} = 0$ has purely twisting parity. This low k_y MTM has a $C_{tear} = 0.7$ indicating that this is indeed a predominantly tearing mode.

The perturbations in $A_{||}$ allow for a magnetic island to form across which particles can move freely. When several islands begin to overlap, the electrons are free to move along the perturbed fields lines off of their equilibrium flux surface. This can result in significant electron heat transport and is given as a potential reason for the high ratio of T_i/T_e often seen in STs [21, 22].

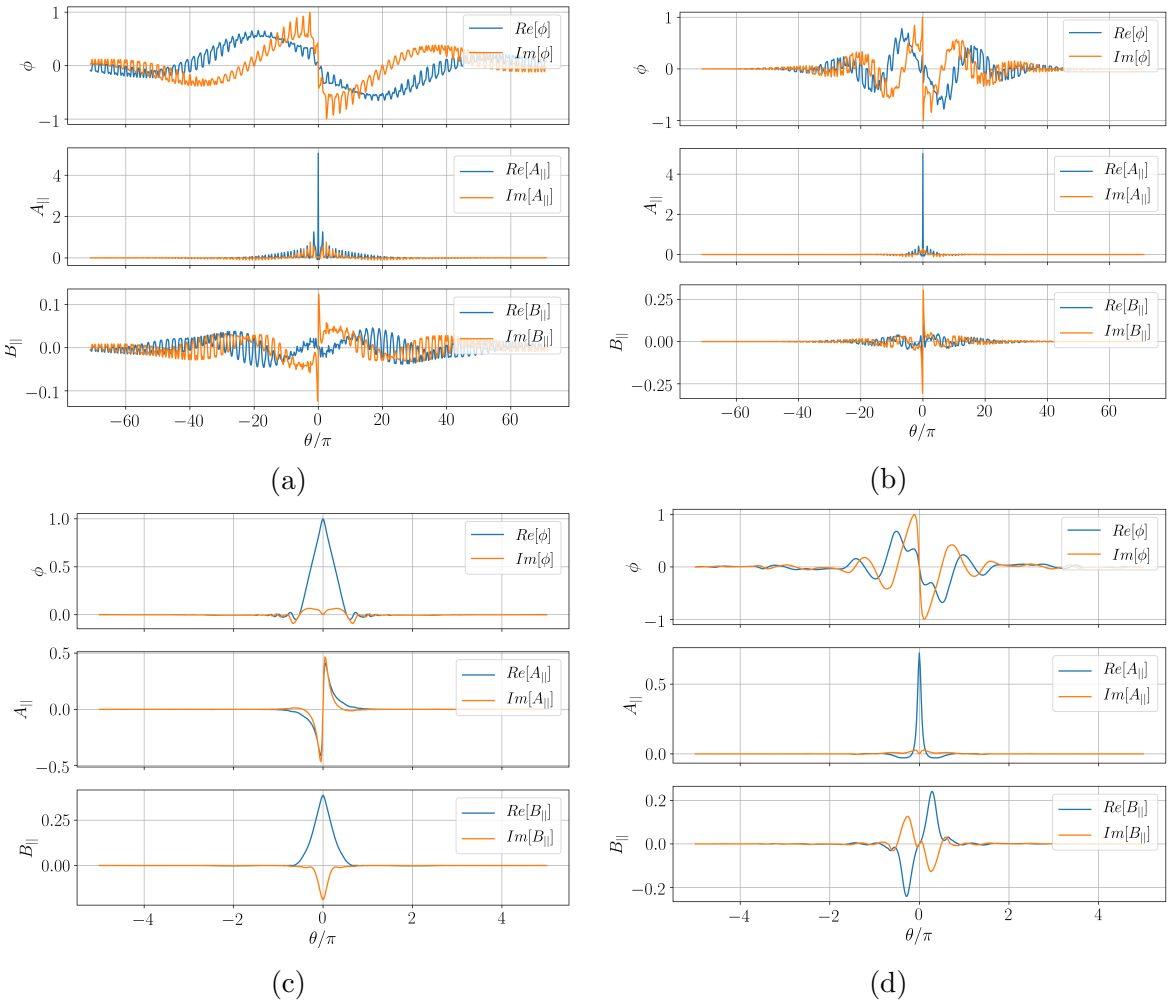

Figure 4: Eigenfunctions for the MTM at $k_y =$ a) 0.1, b) 0.35, c) the KBM at $k_y = 0.35$, and d) the MTM at $k_y = 4.2$ for the $\rho_\psi = 0.5$ surface.

The eigenfunctions of the MTM at $k_y = 0.1$ is shown in Figure 4a. The eigenfunctions have been normalised to the maximum value of $|\phi|$, indicating that the $A_{||}$ fluctuation is significantly larger than the electrostatic fluctuations at $\theta = 0$. Furthermore, these MTMs were found without $B_{||}$ fluctuations which is typical for these modes. The eigenfunction at $k_y = 0.35$ is shown in Figure 4b and it is significantly less extended compared to the $k_y = 0.1$ mode shown in Figure 4a, given that $k_{||} \propto k_y$.

Interestingly, these MTMs were unstable with only $A_{||}$ (both ϕ and $B_{||}$ turned off), adiabatic ions, and without contributions from the trapped particles. This indicates that the important physics lies within the passing electrons. Moreover, these MTMs required collisions suggesting their relevance in the drive of these modes. Furthermore, if the ∇B and curvature drifts were turned off the mode went stable even if the drive for these MTMs was increased, suggesting it wouldn't exist in a slab geometry. This differentiates it from the MTMs derived in Drake *et al* [23] which assumed no toroidal effects, though Rafiq *et al* [24] performed a similar derivation including these effects.

There appears to be two scales at work here, a broad oscillation in θ, and a much narrower oscillation in θ which corresponds to a single poloidal revolution due to the equilibrium variation. With such extended modes, the parallel electron dynamics will be playing an important role as the ions would not be able to travel that far down the field line due to their lower velocity. The extended nature of the mode in ballooning space required a parallel domain from $-71\pi \rightarrow 71\pi$, corresponding

to $k_x = k_y \hat{s}\theta = 26.1$. Even linearly resolving such modes becomes computationally expensive. This suggests that nonlinear simulations may require going out to electron scales in k_x, indicating the potential challenge of fully resolved nonlinear simulations. Similar extended MTM eigenfunctions have been seen in simulations of MAST and NSTX discharges [25, 26].

There are several mechanisms that can drive a MTM. The first is from a parallel thermal force arising from the different frictional forces experienced by electrons travelling in opposite directions along a temperature gradient. This generates a parallel current which in turn generates a perturbation in $A_{||}$ [27]. It was found that this mechanism could be examined in different limits and in the collisionless regime ($\nu_{ee} < \omega$) this thermal force vanishes [23]. For this equilibrium, $\nu_{ee} = 0.017 c_s/a$, which is well below the mode frequency where $\omega \sim 0.5 c_s/a$, suggesting this mechanism is not expected to be relevant.

Another mechanism proposed by Catto & Rosenbluth is where electrons close to the trapped-passing boundary can easily scatter across it, which increases the effective collisionality allowing for a destabilising current driving the tearing instability. This is valid when $\nu_{ee} < \varepsilon\omega$ [28], which is satisfied in this collisionality regime.

Both of these descriptions require a finite collisionality. However, this is not a complete description of MTMs as there are cases where the MTMs don't follow these two descriptions [29]. For example, collisionless MTMs have been found [30–32], though the mechanisms here are not completely understood.

The KBM eigenfunction, shown in Figure 4c, is significantly less extended compared to the low k_y MTM, only extending a single poloidal revolution. The $B_{||}$ perturbation has a significant amplitude and without $B_{||}$, these KBMs are not driven unstable which has been seen before in high β NSTX-like simulations [33]. This KBMs are completely ballooning as they had $C_{tear} = 0.0$. Traditionally, KBMs drive similar levels of electron and ion heat transport as well as significant particle transport differentiating them from MTMs [34].

From $3.0 < k_y < 7.0$, a higher k_y MTMs is seen with the eigenfunction at $k_y = 4.2$ shown in Figure 4d. This mode is also tearing as $C_{tear} = 0.5$. These are much less extended than the MTMs seen at lower k_y but further indicate that multi-scale nonlinear simulations may be necessary. Again, $B_{||}$ has little effect on these modes. Above $k_y = 7.0$ all the modes were found to be stable which suggests that ETG-like modes may not be significant for this equilibria. The cause of the stability is examined in more detail in Appendix Appendix B.

3.2. Impact of flow shear

Flow shear has been shown to stabilise turbulence by shearing the modes. Linearly this corresponds to adding a k_x time dependence to the modes. The effectiveness of flow shear stabilisation can thus be determined by examining how the stability varies with θ_0, as $k_x = k_y \hat{s}\theta_0$ as flow shear will act to advect the mode through θ_0 [35].

A scan was done from $\theta_0 = -\pi \rightarrow \pi$ at $k_y = 0.35$ to determine the impact of flow shear on the low k_y modes. It is only possible to force an odd or even solution when the system is up-down symmetric, so only the dominant mode can be examined with GS2 initial value simulations when $\theta_0 \neq 0$.

Figure 5a illustrates how the KBM growth rate is very sensitive to θ_0 and is quickly stabilised as θ_0 moves away from zero. This suggests that flow shear will help to stabilise the KBMs and act to increase their critical gradient.

However, Figure 5a shows the MTM growth rate is largely unaffected by variations in θ_0 implying that flow shear would have little impact on the mode. The eigenfunction for $\theta_0 = \pi$ is shown in Figure 5b and the same MTM structure is seen. Even when the mode is on the inboard side where the curvature is good, the mode is unstable. This indicates that the drifts reversal, which can occur at the outboard side, may not impact these modes.

These results demonstrate that there is a balance between KBMs and MTMs in this region. A small amount of flow shear will reduce the impact the KBM has on the transport as the mode will spend very little time in the region that is KBM unstable. However, the MTM which persists across θ_0, will likely contribute significantly to the fluxes regardless of flow shear. This is illustrated in Figure

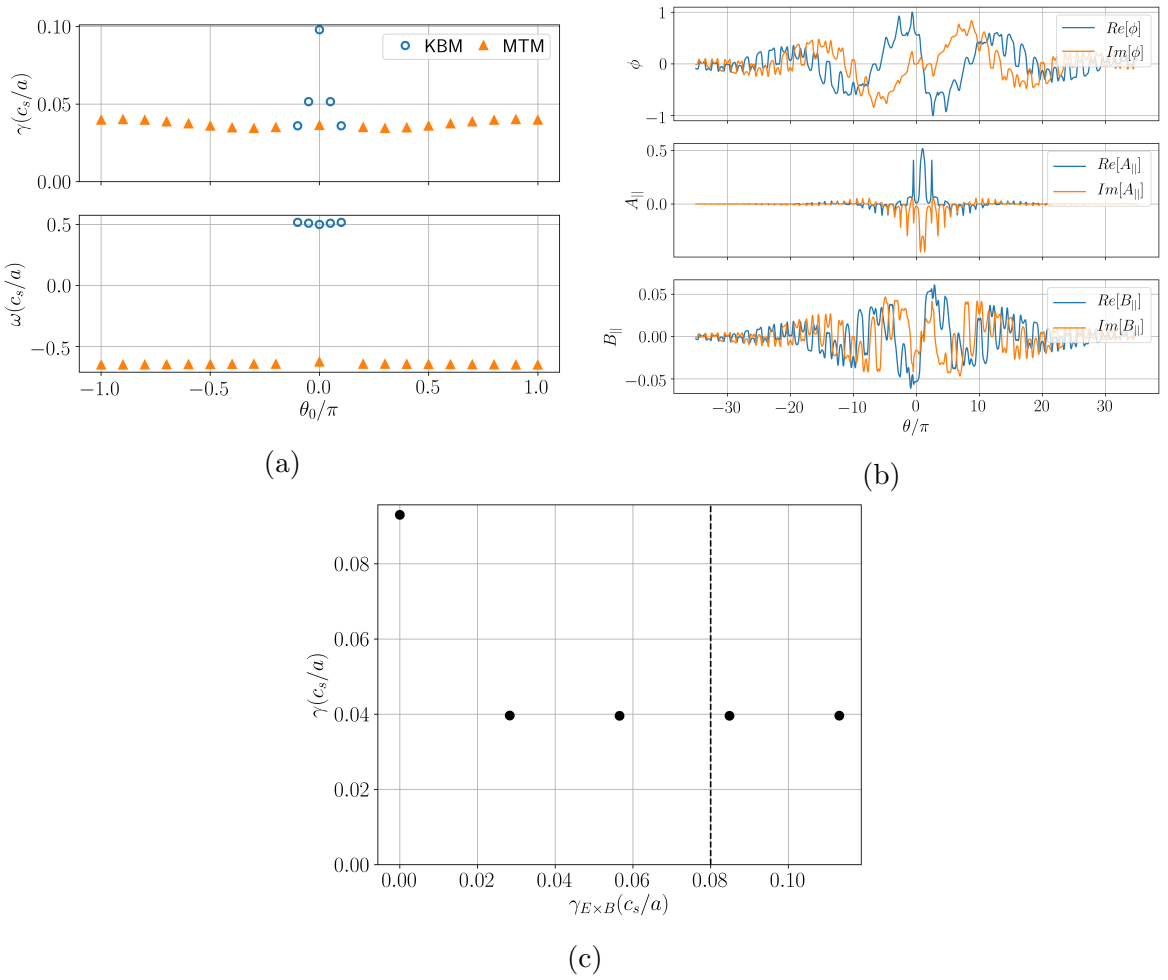

Figure 5: a) θ_0 scan for $k_y = 0.35$ showing the narrow narrow nature of the KBM and the unaffected MTMs. b) The MTM eigenfunction when $\theta_0 = \pi$. c) Effective growth rate when including flow shear where the vertical black line represents the diamagnetic flow shear γ_{dia}.

5c, where $\gamma_{E\times B}$ is included for this simulation. The vertical dashed black line shows diamagnetic flow shear level γ_{dia} [25]. With no flow shear the effective growth rate (black circles) is that of the KBM's growth rate $\gamma = 0.093 c_s/a$. This is stabilised to some extent by a small amount of flow shear, but the effective growth rate remains at the MTM's level of $\gamma \approx 0.04 c_s/a$.

This type of scan was then repeated for the high k_y MTM. Figure 6a illustrates this MTM has a narrow peak in γ around $\theta_0 = 0$, indicating that it will also be stabilised by a small amount of flow shear.

However, a different tearing parity mode appears at $\theta_0 = \pm\pi$ that rotates in the ion diamagnetic direction but has an odd parity ϕ about $\theta_0 = \pi$. The eigenfunction is shown in Figure 6b and it has $C_{tear} = 0.9$, making it more tearing than the MTM situated around $\theta_0 = 0$. This is labelled as an iMTM (grey filled hexagons) and a tearing ion direction mode has not been reported in the literature before (to the best of the author's knowledge), especially one that has a maximum growth rate on the inboard side. This highlights the exotic nature of this equilibrium.

Between $0.1\pi < |\theta_0| < 0.7\pi$, both modes are stable. Including flow shear will move the modes through the stable region, resulting in a lower overall growth rate. Figure 6c shows that the inclusion

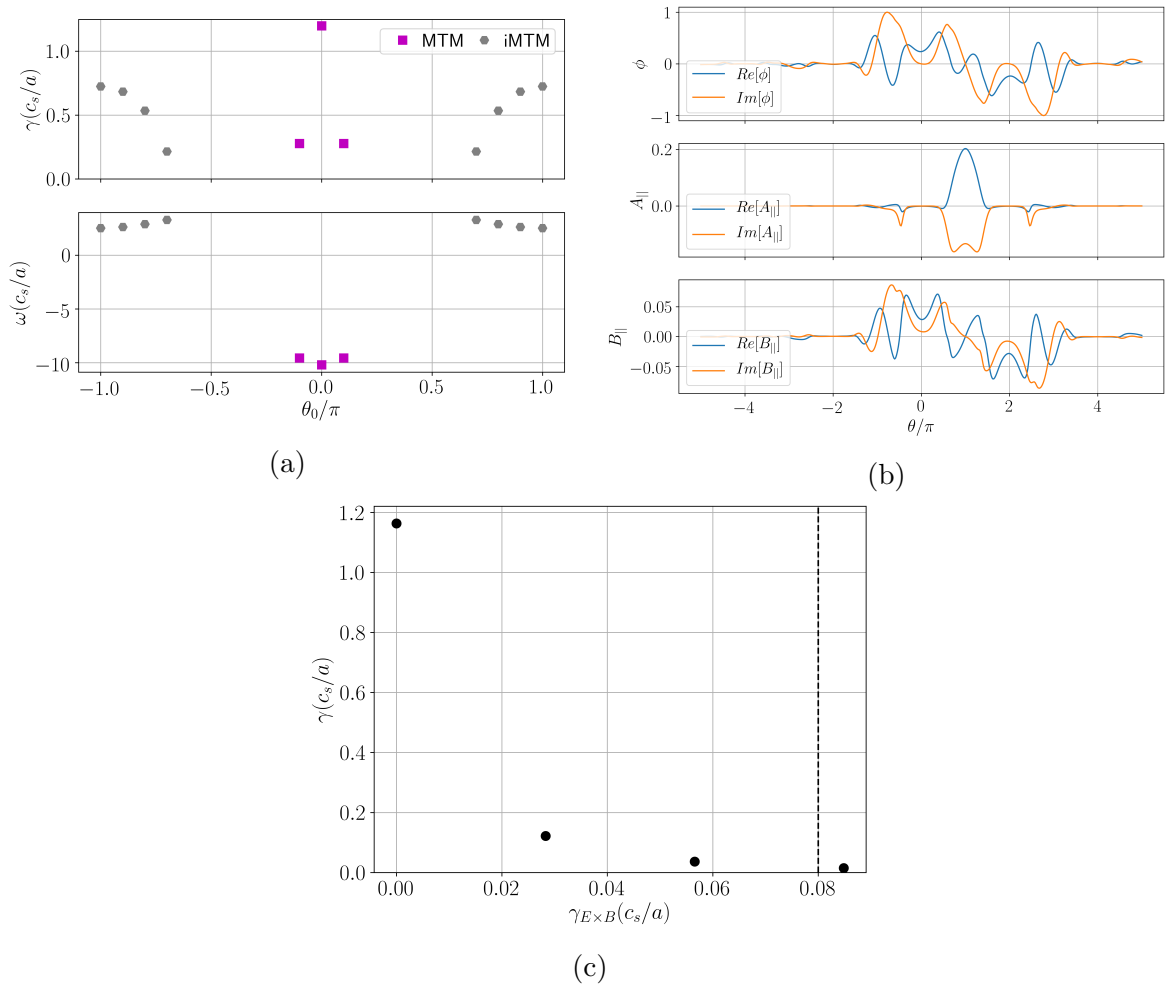

Figure 6: a) θ_0 scan of the dominant mode at $k_y = 4.2$, b) eigenfunction for the inboard iMTM and c) effective growth rate with $E \times B$ shear. The vertical black line shows γ_{dia}.

of flow shear reduces the effective growth, even for very low values of $\gamma_{E\times B}$, such that at diamagnetic levels of flow shear the mode is close to stable. A $\gamma/k_\perp^2$ argument would suggest that the impact of these MTMs on the total transport may not be significant.

This motivates the equilibrium being modified such that the low k_y MTMs are stabilised given that the KBMs and high k_y MTMs will likely be stabilised by flow shear.

4. Parametric dependence of micro-instabilities

The rest of this work aims to understand what drives these modes such that the equilibrium can be re-designed to help stabilise them. The parametric dependence of the linear modes will be determined which will help identify which plasma parameters are relevant for these modes and should be the focus of optimisation. Using this information it will be possible to determine a route to stabilising the low k_y MTMs while assuming the KBMs and high k_y MTMs aren't driven significantly more unstable, so that they can be largely ignored when optimising the equilibrium. An important open question, beyond the scope of this work, is how the plasma transitions from a state where the KBM is dominant to one where the MTM is dominant, and the impact on the transport.

4.1. Impact of kinetic profiles

In SCENE, the density and temperature profiles are prescribed, meaning the main transport assumption is quantified via the H_{98} and H_{Petty} scaling laws. This sub-section will investigate the impact the kinetic profiles will have on the modes found thus far. Changing the kinetic profiles will change the kinetic gradients a/L_n and a/L_T, so the impact of these needs to be quantified to identify desirable operating scenarios. In this section the electron and ion temperature gradient will be independently changed to explore their impact on the KBMs and MTMs. Next the density gradient of the electrons and ions will be scanned together such that quasi-neutrality is maintained.

In the gyrokinetic equation, the pressure gradient appears in two separate terms, the equilibrium pressure gradient (used to define the perpendicular drift velocity) and the gradient drive term. Usually in gyrokinetic codes, it is possible to define these terms independently allowing for the impact of those terms to be isolated. In GS2 the equilibrium pressure gradient is defined by $\beta'_{e,unit} \equiv -\beta_{e,unit} a/L_p$ where $a/L_p = \sum_s \frac{n_s T_s}{n_{ref} T_{ref}}(a/L_{Ts} + a/L_{ns})$. The kinetic gradients for each species are defined separately and for a fully consistent calculation these two terms should match. In this section the equilibrium was maintained by keeping $\beta'_{e,unit}$ fixed, whilst inconsistently changing the kinetic gradients, allowing for the impact of the kinetic gradients to be isolated§.

Changing the density and temperature profiles will also impact the collisionality as $\nu_* \propto n_s/T_s^2$, so a higher density, lower temperature scenario will have a higher collisionality. Furthermore, the impact of impurities and fast ions will be important. This work won't include an impurity species, but will investigate the impact Z_{eff} has on these modes. Examining the impact of fast ions such as fusion α's is left as future work.

4.1.1. Electron Temperature gradient The impact of the electron temperature gradient was examined by scanning from $a/L_{Te} = 0 \rightarrow 7.0$ at $k_y = 0.35$. It is expected that this will have a significant impact on all the modes seen thus far, as MTMs are traditionally driven unstable by the electron temperature gradient and KBMs are driven unstable by the total pressure gradient. The eigenvalues are shown in Figure 7a, with the reference equilibrium value shown with the vertical black dashed line.

There appears to be a critical gradient where the KBM is completely stable at $(a/L_{T_e})^{KBM}_{crit} = 2.0$, corresponding to $a/L_p = 5.63$. Its growth rate increases exponentially with a/L_{Te} which may lead to stiff transport and if γ becomes sufficiently large then the flow shear stabilisation may not be sufficient in suppressing the transport. The mode frequency is dropping as the temperature gradient increases. It seems a small drop in the a/L_{T_e} would allow for the MTM to become the dominant instability.

Looking at the dominant odd eigenmode, it can be seen that there's a critical gradient $(a/L_{Te})^{MTM}_{crit} = 1.0$. This critical gradient may be the limiting factor on the electron temperature profile as MTMs can drive significant electron heat flux. The mode frequency scales with the temperature gradient and this follows predictions made by Catto and Rosenbluth [28], which predicted that the mode frequency of an MTM is given by $\omega^{CR}_{MTM} \sim \omega^*_e[1 + \eta_e/2]$ where ω^*_e is the electron diamagnetic frequency defined as $\omega^*_e = k_y(a/L_{ne})$ and $\eta_e = (L_{ne}/L_{Te})$. The orange dashed line shows ω^{CR}_{MTM}, indicating that this scaling fits well.

The MTM growth rate has a much weaker dependence on the a/L_{Te} compared to the KBM and actually appears to level out, suggesting that small changes made to the electron temperature gradient may not have an impact on the transport. At sufficiently high gradient the MTM gets stabilised, this has been seen before in MAST simulations [29] where MTMs also followed ω^{CR}_{MTM}. This was thought to be related to a resonance with a drift frequency. If $|\omega|$ is increased sufficiently then this resonance is disturbed and the mode becomes damped. This bifurcation could lead to a scenario where the high temperature gradient is actually stabilising if it is possible to push through the lower gradient regime.

§ β' is related to the parameter α often used to define the pressure gradient with $\alpha = Rq^2\beta'$ in the infinite aspect ratio shifted circular geometry

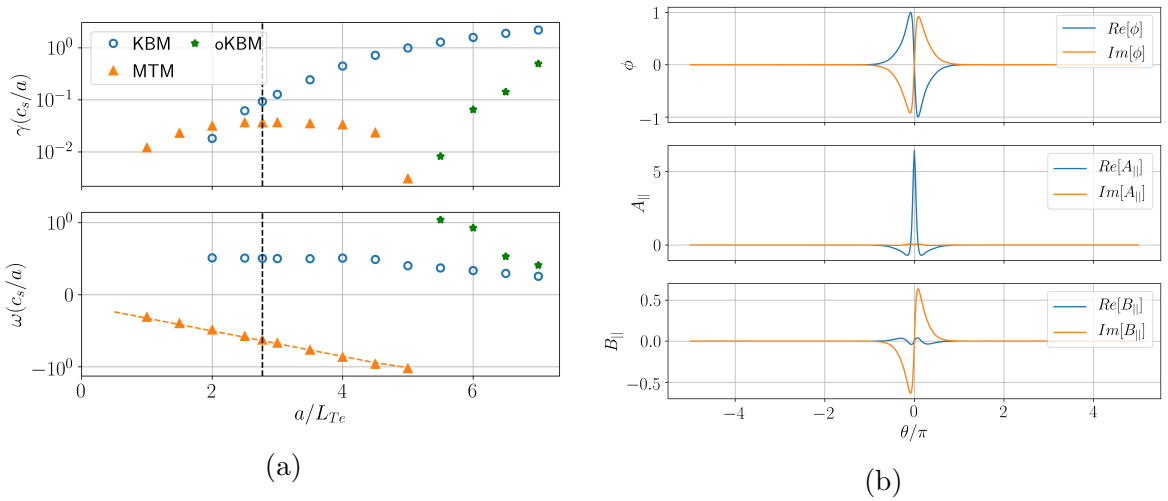

(a) (b)

Figure 7: a) Examining the impact of plasma a/L_{Te} when $k_y = 0.35$. The dominant even (KBM) and odd (MTM) instabilities are shown, with the KBM demonstrating much stiffer behaviour. Note the log scale in γ. The dashed line shows the analytic prediction ω^{CR}_{MTM} defined in the text. b) Eigenfunction of for the ion direction mode (filled green stars) for $a/L_{Te} = 7.0$; despite being odd parity, the mode is not tearing as $C_{tear} = 0.0$.

However, when $a/L_{Te} > 5.0$, an ion direction mode emerges that has an odd ϕ eigenfunction, shown in Figure 7b. Its frequency is tending towards the KBM frequency. This however, is not a tearing mode as it has $C_{tear} = 0.0$. This rather appears to be an odd parity KBM, which will be labelled as an oKBM and will be represented with the filled green stars as seen in Figure 7a. This oKBM is a higher order eigenstate of the KBM and has been seen before in steep-gradient simulations [36]. Any quasi-linear model may need to account for this extra source of transport. Access to these temperature gradients may be possible if these oKBMs are also stabilised by flow shear, but the level of transport driven by the MTM must first be quantified. If this is an oKBM, it should be seen when scanning through a/L_{Ti}.

It is expected that the high k_y MTMs will be impacted by a/L_{Te} so a similar scan is shown in Figure 8 for $k_y = 4.2$. Once again non-monotonic behaviour is seen. The critical electron temperature gradient occurs at $a/L_{Te} = 1.0$, similar to the lower k_y MTM seen earlier. It peaks at $a/L_{Te} = 3.5$ and then begins to drop off. Significant changes would be required to stabilise this MTM, though given the flow shear stabilisation it is not expected to play a significant role in transport.

4.1.2. Ion temperature gradient A similar scan was performed for the ion temperature gradient by scanning from $a/L_{Ti} = 0 \rightarrow 7$ whilst keeping the other kinetic gradients fixed. For $k_y = 0.35$, the KBM and MTM eigenvalues are shown in Figure 9. The KBM has a similar critical gradient to the previous scan with $(a/L_{Ti})^{KBM}_{crit} = 2.0$, as expected if the relevant parameter is a/L_p. Once again the KBM is strongly destabilised by a/L_{Ti} and the mode frequency in this case actually increases with a/L_{Ti}, which suggests that the KBM frequency scales like η_i/η_e.

Examining the low k_y MTM, its growth rate and mode frequency are largely unaffected by a/L_{Ti} as expected. Once again if the ion temperature gradient is pushed high enough then when $a/L_{Ti} > 5.5$ an oKBM appears at a similar threshold as the a/L_{Te} scan. The high k_y MTM is also unaffected by the ion temperature gradient.

It has been found in MTM driven transport, that 98% of the heat transport can occur in the electron channel [16]. This suggests that a/L_{Ti} will predominantly be limited by the the electron-ion

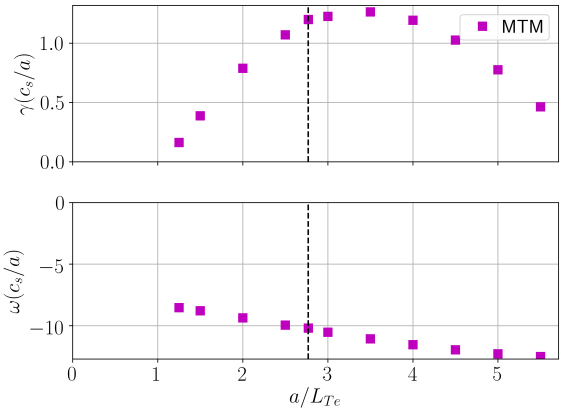

Figure 8: Examining the impact ofa/L_{Te} on the MTMs at $k_y = 4.2$.

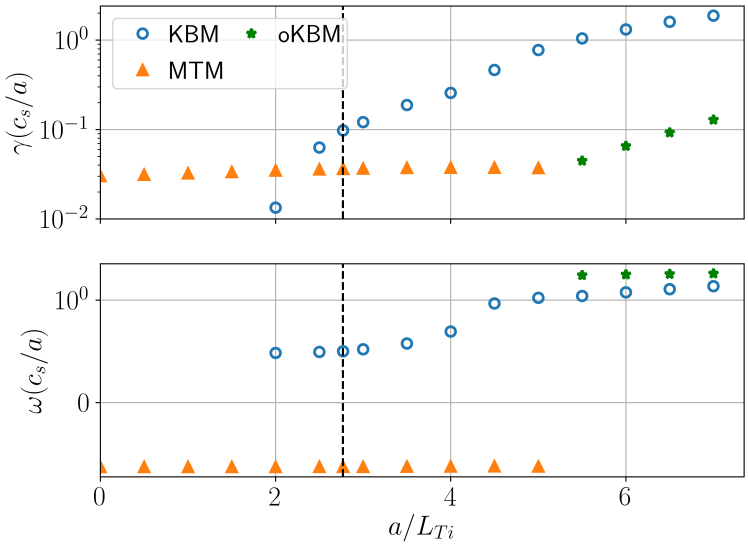

Figure 9: Examining the impact of plasma a/L_{Ti} when $k_y = 0.35$. The dominant even (KBM) and odd (MTM) instabilities are shown, with the KBM demonstrating much stiffer behaviour. The oKBM is again found at high a/L_{Ti}.

exchange power assuming the KBMs is suppressed by flow shear.

4.1.3. Density gradient A density gradient scan was performed from $a/L_n = -1 \rightarrow 1$, corresponding to $a/L_p = 3.54 \rightarrow 7.54$, and it can be seen from Figure 10a that when increased the KBM is destabilised, which further supports that fact that this is a pressure gradient driven mode. The KBM is stable when $a/L_n < 0$ corresponding to $a/L_p = 5.54$ which is similar to the critical value in the temperature gradient scan. The mode frequency is unaffected which supports the idea that ω_{KBM} scales with η_i/η_e which remains unchanged in this scan. When the density gradient is negative the KBM is stabilised and a TEM (hollow red diamonds) appears, though this is a scenario that should be avoided.

The low k_y MTM seems to be stabilised by a large $|a/L_n|$, which has been seen before on NSTX [26] and on MAST [15]. This again was thought to be due to the mode frequency changing and disrupting a resonance, though the peak growth rate here occurs as $\omega = 0.4c_s/a$ and in the a/L_{Te} scan it occurred at $\omega = 0.6c_s/a$.

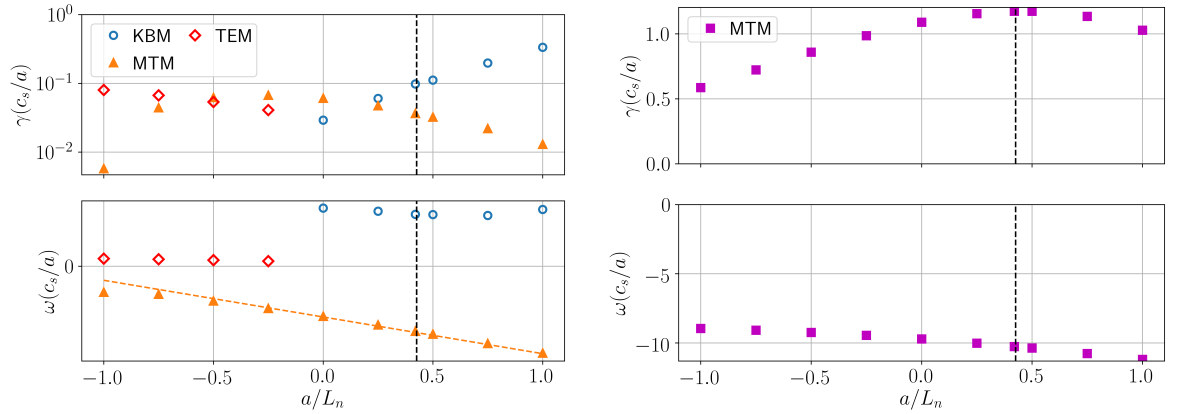

Figure 10: Examining the impact of a/L_n when a) $k_y = 0.35$ and b) $k_y = 4.2$. The dominant even (KBMs and TEMs) and odd (MTM) instabilities are shown, with the KBM demonstrating much stiffer behaviour.

For the high k_y MTMs, the equilibrium happens to lie at the peak of the growth rate spectrum so increasing the density gradient would help to stabilise the mode, but the effect is not as large compared to the impact on the low k_y MTMs. Given the similar behaviour as the low k_y modes, similar measures can be taken to stabilise these modes, noting that their impact on transport will not be as significant given the flow shear stabilisation.

4.1.4. Total pressure gradient It has been shown that increasing any of the kinetic gradients drives the KBM unstable. Assuming the KBM is driven by the total pressure gradient, if the total pressure gradient is kept fixed a similar growth rate should be seen. However, if the temperature gradient is exchanged for density gradient then it should be expected that the MTM will be stabilised. This should be doubly beneficial for the stability as the drive from a/L_{Te} is reduced and the stabilisation from a/L_n is being increased. A scan was performed at fixed a/L_p where the density gradient was changed from $a/L_n = 0 \rightarrow 1.5$ and $a/L_{Te} = a/L_{Ti}$ was set. The eigenvalues are shown in Figure 11. It can be seen that the MTM is indeed stabilised, and when $a/L_n > 1.0$, the MTM is completely stable.

This critical gradient occurs at the same value as the pure density gradient scan, indicating that reducing the electron temperature gradient is not having an impact on the MTM growth rate. This is explained by the "levelling" out of the MTM growth rate seen in Figure 7a during the a/L_{Te} scan, indicating that small changes in a/L_{Te} will not impact these MTMs significantly.

Overall, this implies that a peaked density profile could be beneficial in reducing MTM-based transport. The KBM is also stabilised slightly indicating it has a stronger dependence on the temperature gradient. Moreover, this scan maintains a consistent equilibrium as the Grad-Shafranov equation doesn't differentiate between density and temperature when accounting for the pressure.

4.1.5. Collision Frequency The kinetic profiles were specified to generate $P_{fus} = 1.1GW$, but it would be possible to operate at a higher density and lower temperature at the same fusion power. This would directly impact the collisionality of the plasma given that $\nu_* = \nu_{ee}/\varepsilon\omega_b$ and $\nu_{ee} \propto n_e/T_e^{3/2}$‖.

MTMs are generally reported to be highly sensitive to the electron collision frequency, so a scan was conducted from $\nu_{ee} = 0 \rightarrow 0.14c_s/a$ and ν_{ei} was consistently changed assuming $T_e = T_i$. An electron collision frequency of $0.14c_s/a$ (which corresponds to $\nu_* = 0.05$) is rather high for reactor

‖ Due to the c_s/a normalisation used, then the collision frequency parameter will actually scale like n_e/T_e^2

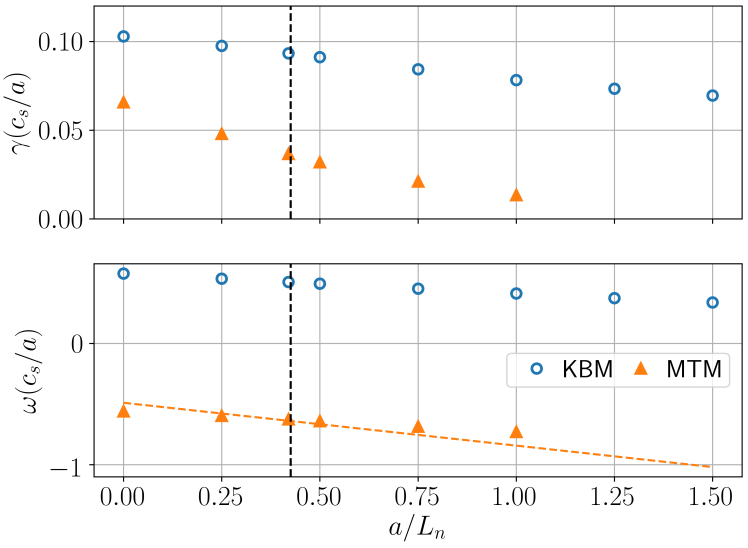

Figure 11: a) A scan was performed at fixed a/L_p where the contribution of a/L_n was varied for $k_y = 0.35$. $a/L_{Te} = a/L_{Ti}$ was enforced.

relevant conditions and would be approximately at the Greenwald limit for this device. Given the high temperatures of a reactor, it will be difficult to operate at a significantly higher collision frequency.

When examining the low k_y MTM, as shown in Figure 12a, it appears that collisions are necessary and destabilising for this mode. Note the linear scale here. Additionally, the collisions reduce the extent of the mode in ballooning space as shown in Figure 12b where $\nu_{ee} = 0.14 c_s/a$. This is due to the passing electrons undergoing a collision before they can propagate further along the field line. The reduced extent of the mode would make nonlinear simulations easier to resolve. As the collision frequency is dropped towards 0, the MTM growth rate tends to 0.

This suggests that the confinement will scale favourably as collisionality is reduced, aligned with previous confinement scaling laws in STs where $B\tau_e \propto \nu_{*e}^{-0.82}$ [37]. One conclusion is that to reduce the electron transport a low collisionality regime is favourable.

However, Figure 12a also shows that as the collision frequency is increased the KBM is stabilised and a similar feature has been seen in a hybrid TEM/KBM mode in simulations of NSTX [16]. There is a critical collision frequency at which the dominant mode switches from a KBM to a MTM and the KBM becomes stable for $\nu_{ee} > 0.12 c_s/a$.

Examining the impact of collisions on the high k_y MTM, it can be seen from Figure 12c that these are collisionless MTMs, highlighting the completely different nature of these modes compared to the longer wavelength MTMs. Collisionless MTMs have been seen before [30–32, 38], but their mechanism is not fully understood. These are stabilised by collisions, but it appears that the impact is not significant.

A scenario can be imagined where due to the large electron transport, the temperature gradient will drop, stabilising the MTM. However, the lower electron gradient will also lower the temperature and increase the collisionality which could drive the MTM even more unstable. This bootstrapping process could result in very low plasma temperatures. Conversely, if electron heating is sufficient to get over the peak growth rate for the MTM such that increasing a/L_{Te} is stabilising for these MTM, then this feedback loop is positive. This could lead to a bifurcation to a high a/L_{Te}, high confinement regime.

Finding an equilibrium point between the lowered a/L_{Te} and higher ν_{ee} will be critical in determining the electron temperature. This can then in turn impact the ion temperature through the collisional exchange power.

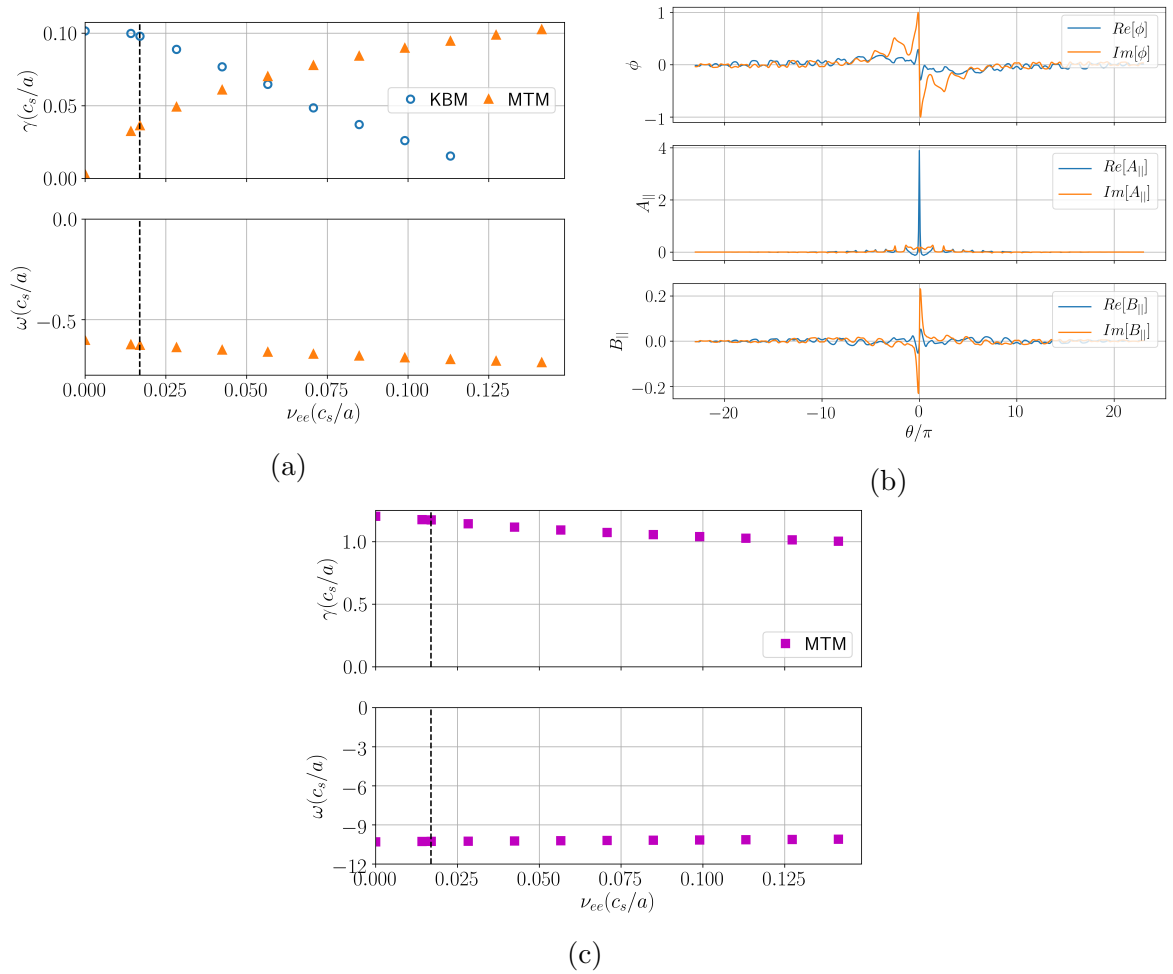

Figure 12: a) Impact of collision frequency showing the dominant odd and even parity mode for different values of ν_{ee} when $k_y = 0.35$. Note the linear scale here. b) the eigenfunction when $\nu_{ee} = 0.14 c_s/a$. c) $k_y = 4.2$

Previous work has also found Z_{eff} to be destabilising for MTMs, via its impact on the collision frequency as $\nu_{ei} \rightarrow Z_{\text{eff}}\nu_{ei}$ in the Lorentz collision operator [16, 26]. The simulations conducted thus far had $Z_{\text{eff}} = 1.0$, but in reality there will be impurities and helium in the plasma, raising the Z_{eff}. STPP was designed with an assumed $Z_{\text{eff}} \approx 1.6$, so it is crucial to quantify the impact it may have. A scan was performed from $Z_{\text{eff}} = 1.0 \rightarrow 2.0$. It should be noted that impurities were not included in the simulation such that Z_{eff} is being inconsistently set. This only has an impact on the collision operator. Figure 13 illustrates the dependency on Z_{eff}, with a doubling of Z_{eff} causing the MTM growth rate to increase from $0.36 \rightarrow 0.51 c_s/a$. A similar growth is seen when the collision frequency is doubled instead where $\gamma = 0.54 c_s/a$, which further confirms how Z_{eff} acts to increase the effective collision frequency between the ions and electrons, which drives the MTM. Moreover, when removing electron-electron collisions the mode was unaffected, further highlighting that electron-ion collisions are the relevant drive for this MTM. Figure 13 indicates the KBM growth rate is weakly stabilised, similar to the ν_{ee} scan. In summary, any impurities in the plasma would cause a slight downshift in the MTM critical gradient.

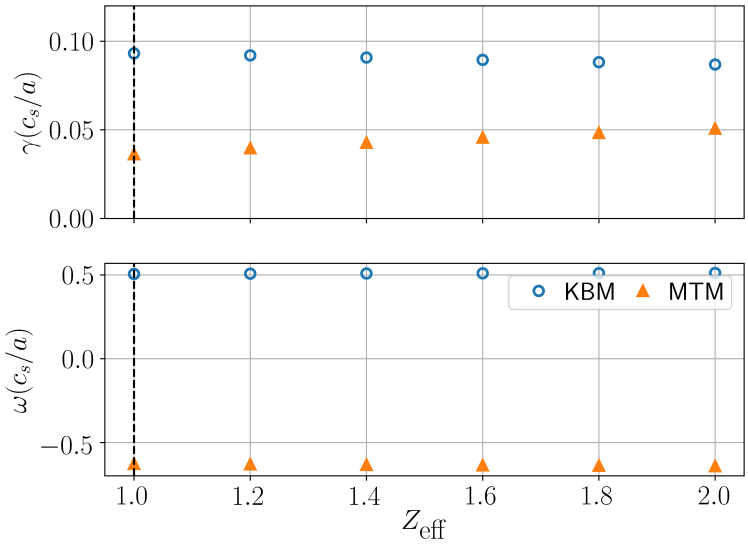

Figure 13: Examining the impact of Z_{eff} on the KBMs and MTMs for $k_y = 0.35$ and $\nu_{ee} = 0.14 c_s/a$.

4.2. Magnetic equilibria

Both MTMs and KBMs are inherently electromagnetic modes, so the total magnetic field will have a significant impact on the modes via β_e. Furthermore, there is evidence that both of these modes are impacted by both q and $\hat{s}$, which are set by the field and current profile. Both of these were also inputs to SCENE, so it is possible to vary the assumptions about the magnetic equilibrium to see how to further stabilise these modes. This section will give an indication of how changing I_{rod}, I_p and the auxiliary current J will impact these modes.

4.2.1. Impact of $\beta_{e,unit}$ and $\beta'_{e,unit}$ The plasma β can be reduced by increasing I_{rod} and I_p at fixed fusion power. Increasing the central rod current is limited by the engineering limits of regular conductors like copper and aluminium. Turning to superconductors may help to increase the toroidal field but will complicate the design with the additional shielding required.

A scan was conducted in $\beta_{e,unit} = 0.0 \rightarrow 0.024$ at $k_y = 0.35$, where $\beta_{e,unit} = 0.024$ at $\rho_\psi = 0.5$ approximately corresponds to a 40% drop in the field compared to the reference case in Table 2. This must be explored carefully as changing $\beta_{e,unit}$ would in turn change $\beta'_{e,unit}$ and as mentioned previously in GS2 it is possible to inconsistently change $\beta_{e,unit}$ and $\beta'_{e,unit}$. Firstly $\beta'_{e,unit}$ is kept fixed at the equilibrium value and this is shown in Figure 14a.

Looking at the even modes, when $\beta_{e,unit} = 0$, a weakly unstable TEM appears. Above a critical value of $\beta_{e,unit} = 0.01$, the KBM mode becomes unstable, before it begins to saturate around $\beta_{e,unit} = 0.02$. Looking at the MTMs, again there is a critical $\beta = 0.006$, below which the MTM is stable. This is driven unstable by $\beta_{e,unit}$, but when $\beta_{e,unit}$ increases sufficiently then the oKBM is seen, which is very sensitive to $\beta_{e,unit}$ and quickly begins to approach the KBM growth rate.

$\beta'_{e,unit}$ is used to calculate the equilibrium and has large impacts on the magnetic drifts and local current. A scan was performed in $\beta'_{e,unit}$ at the fixed equilibrium $\beta_{e,unit}$ to isolate its impact. This is shown in Figure 14b where it can be seen that at low $\beta'_{e,unit}$, the KBM/oKBM are the dominant instabilities. These are quickly stabilised and the dominant odd mode switches from an oKBM into the MTM and the dominant even mode switches from a KBM to a weakly unstable TEM. The MTM is not significantly affected by $\beta'_{e,unit}$ and the reason can be determined by examining the drifts.

Figure 15 illustrates how $\omega_{\nabla B}$ and ω_{curv} are modified by changing $\beta'_{e,unit}$. The total magnetic drift is approximately the sum of $\omega_{\nabla B}$ and ω_{curv}. Here a negative drift frequency corresponds to

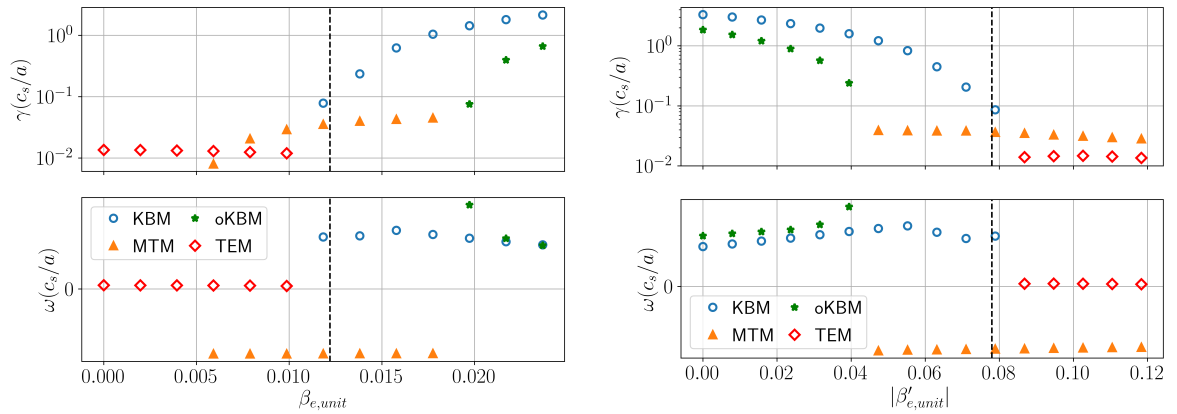

(a) (b)

Figure 14: Examining the impact of a) $\beta_{e,unit}$ at fixed $\beta'_{e,unit}$ and b) $\beta'_{e,unit}$ at fixed $\beta_{e,unit}$ on the linear micro-instabilities at $k_y = 0.35$.

"good curvature" and positive is "bad curvature". Increasing $\beta'_{e,unit}$ makes $\omega_{\nabla B}$ negative such that the combination of the two drifts becomes stabilising on the outboard side, resulting in "good curvature". However, this is only significant when $|\theta| < \pi$, i.e. the first poloidal revolution. For ballooning modes like KBMs, this will be stabilising. For very extended modes, like the MTM, $\omega_{\nabla B}$ is positive on the outboard side after a single poloidal revolution meaning the stabilising effect won't occur. Although the MTMs are weakly stabilised by increasing $\beta'_{e,unit}$, this suggests that the drift reversal won't have a significant impact. This further highlights the need to examine high $\beta'_{e,unit}$ equilibria at various different values of θ_0.

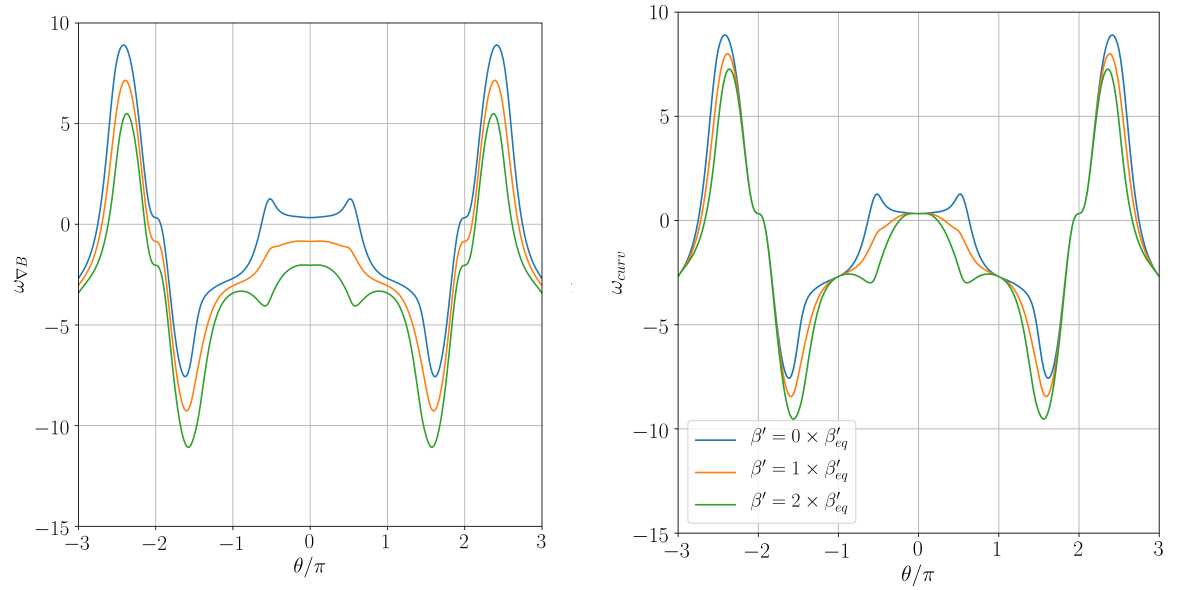

(a) (b)

Figure 15: The impact $\beta'_{e,unit}$ has on $\omega_{\nabla B}$ and ω_{curv}. The ∇B drift is negative for the high β' cases when $|\theta| < \pi$, which is stabilising for ballooning modes.

For the high k_y MTM, Figure 16a shows a scan of changing $\beta_{e,unit}$ at fixed $\beta'_{e,unit}$. Exceeding

a critical $\beta_{e,unit} = 0.003$ was found to destabilise this mode, corresponding to a 70% increase in the field. Below this a weakly unstable TEM is seen. Figure 16b shows how changing $\beta'_{e,unit}$ impacts the MTM which is very different to the low k_y MTMs which were largely unaffected by $\beta'_{e,unit}$. At lower $\beta'_{e,unit}$ this MTM is stabilised, but another MTM appears at $\beta'_{e,unit} = 0$, likely also driven unstable by $\beta_{e,unit}$. At $\beta'_{e,unit} = 0.0$, this MTM has $C_{tear} = 0.3$ which is lower than that for the equilibrium $\beta'_{e,unit}$ at $\theta_0 = 0$ which had $C_{tear} = 0.5$. However, a scenario with a very low $\beta'_{e,unit}$ and high $\beta_{e,unit}$ requires a very low pressure gradient which is not desirable for a reactor.

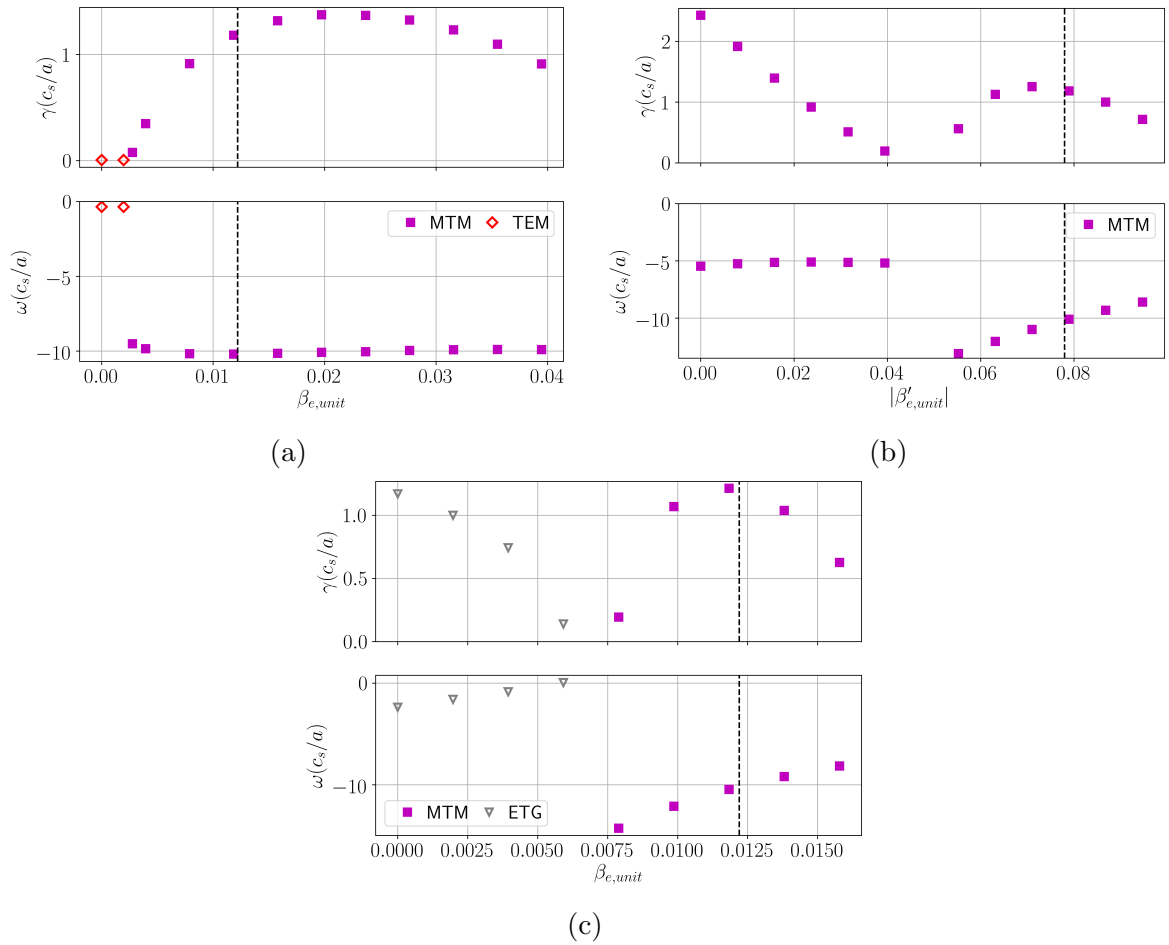

Figure 16: Examining the impact of changing a) $\beta_{e,unit}$ at fixed $\beta'_{e,unit}$ and b) $\beta'_{e,unit}$ at fixed $\beta_{e,unit}$ and c) $\beta_{e,unit}$ and $\beta'_{e,unit}$ together on the MTMs at $k_y = 4.2$.

To examine the relevance of this low $\beta'_{e,unit}$ MTM, a scan was done where $\beta'_{e,unit}$ and $\beta_{e,unit}$ were changed together i.e. $\beta_{e,unit} = \beta_{e,unit} a/L_p$ was maintained throughout this scan. Figure 16c shows that at sufficiently low $\beta_{e,unit}$, the original MTM is stabilised and the new MTM does not appear. However, an ETG mode (hollow grey upside-down triangle) appears when operating at lower $\beta_{e,unit}$ and $\beta'_{e,unit}$. This ETG is explored in more detail in Appendix Appendix B. But this suggests that this low $\beta'_{e,unit}$ MTM will not be relevant.

4.2.2. Safety factor profile The q profile has a large impact on both the MHD and the micro-stability of a reactor. Tailoring the q profile requires careful control of the auxiliary current profile so it may be difficult to optimise it for turbulence but this section highlights how it will impact these modes.

The $n = \infty$ ballooning stability boundary for ideal ballooning modes is often used as an initial indicator for the onset of KBMs [39] and in GS2 there is a module that can calculate this boundary [40].

Figure 17 shows how this ideal stability boundary changes with q, illustrating a somewhat complicated relation between the ideal ballooning mode and q. As q increases the stability boundary moves to high $\hat{s}$ and lower $|\beta'|$. Therefore pushing to a higher q will make access to the second stability region easier. At sufficiently low q, the stability boundary gets pushed to higher $|\beta'|$ enabling the equilibrium to lie in the first stability region.

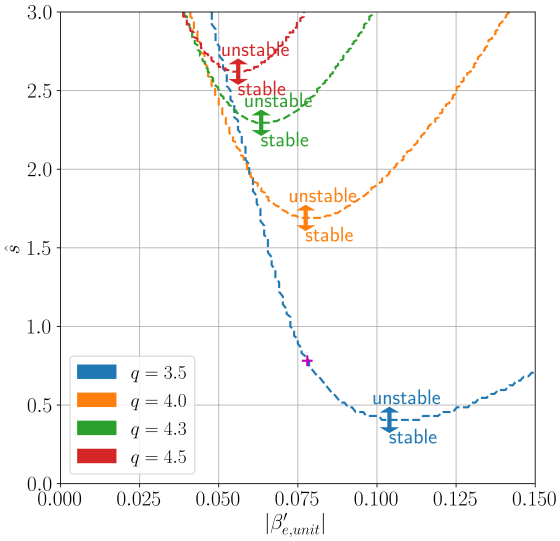

Figure 17: $\hat{s} - |\beta'|$ diagram showing how the the ideal ballooning stability boundary moves with q. The reference equilibrium value of $\hat{s}$ and $|\beta'_{e,unit}|$ is shown by the magenta cross and has $q = 4.3$ (green curve).

Evidently, the ideal ballooning mode is not sufficient in predicting the KBM threshold as it predicts this equilibrium to be stable, but it can give an idea of how the KBM will behave. Figure 18a shows a scan in q for the kinetic modes. For $q < 3.0$, when the equilibrium is in the first stability region, an ITG (hollow cyan pentagons) mode is dominant but as the equilibrium enter the second stability region, the KBM becomes the dominant instability. As q is increased the KBM peaks and then becomes stabilised as the ideal boundary gets pushed further away from the equilibrium value. When the equilibrium is in the second stability region then increasing q stabilises the KBM and a TEM appears, indicating that operating at high q may help to increase the KBM critical gradient.

A scan was also conducted with $\hat{s}$ and Figure 18b shows how the KBM is destabilised by increasing $\hat{s}$, consistent with the ideal ballooning mode behaviour.

Next, the impact $\hat{s}$ and q have on the MTMs is explored, and it can be expected that increasing q will be destabilising for this MTM given that $\nu_* \propto q$. To isolate the impact on the MTM and avoid the oKBM being driven unstable, the q scan was run with $\nu_{ee} = 0.14 c_s/a$. Figure 19a illustrates how there appears to be a linear relationship between q and the MTM growth rate, consistent with a ν_* scaling. The magnetic shear dependency displays non-monotonic behaviour as shown in Figure 19b.

The impact of $\hat{s}/q$ is often examined as it is related to Landau damping and field line bending. For the MTM seen here it appears that $\hat{s}/q$ has a non-monotonic behaviour, so the impact on the turbulent transport will be difficult to predict. This has been seen before on MAST [15]. However, there are examples where $\hat{s}/q$ is stabilising for MTMs like in DIII-D [14] and counter-examples where $\hat{s}/q$ tends to be destabilising, such as on NSTX [26] attributed to higher field line bending. This further highlights the complicated behaviour of MTMs so further work is needed to understand the dependence on q-profile.

Figure 20a shows a scan in q for the high k_y MTMs, and it can be seen that there is a peak in the growth rate at $q = 4.0$, so an increased q will help to stabilise this mode. A higher B_φ device will

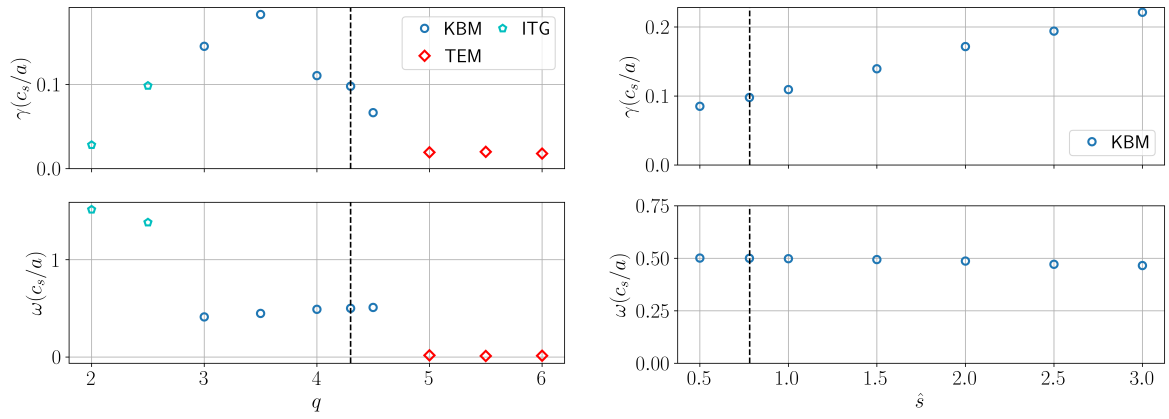

Figure 18: Dominant even mode eigenvalues when changing a) q and b) $\hat{s}$ for $k_y = 0.35$.

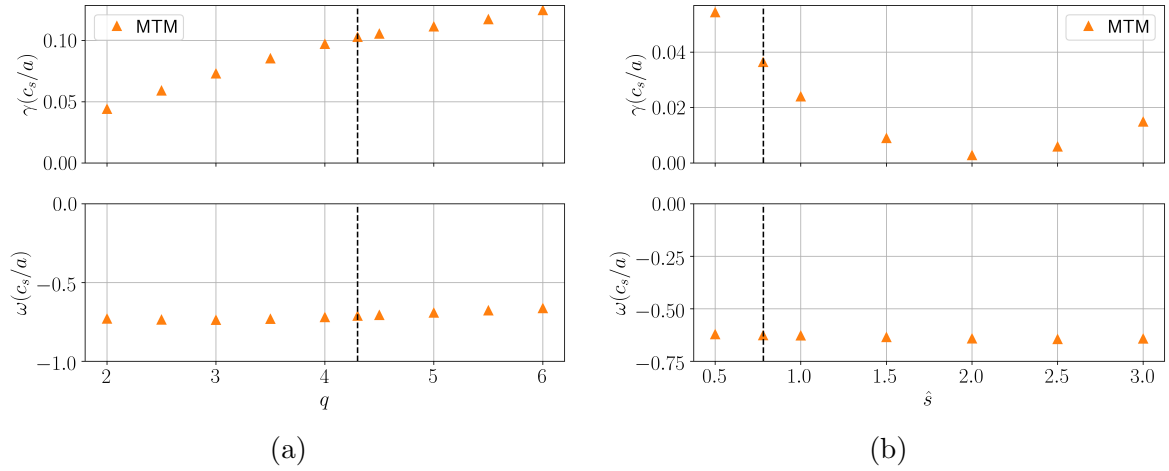

Figure 19: Dominant odd mode eigenvalues when changing a) q (at $\nu_{ee} = 0.14 c_s/a$) and b) $\hat{s}$ for $k_y = 0.35$.

likely have a higher q, so the combination of lower $\beta_{e,unit}$ and higher q indicates that this mode will be stabilised by a higher B_φ. At very high q an iMTM mode with $C_{tear} = 0.7$ was found, though it exists for a very narrow window. Looking at the behaviour with $\hat{s}$ in Figure 20b, there is a non-monotonic dependence similar to the lower k_y MTM. However, it seems to be a weak dependence so will likely not to be significant for this MTM.

This analysis was repeated for two different flux surfaces at $\rho_\psi = 0.3$ and 0.7 and similar KBMs and MTMs were found, indicating that these modes and the trends reported here exist robustly across the whole equilibrium.

5. Options for stabilising the equilibrium

The previous sections have shown potential routes to stabilising the modes found so far. Two routes are taken to see how the micro-stability is impacted. Firstly, the impact of increased toroidal field is examined. It would also be possible to increase the plasma current, but that comes at the cost of additional auxiliary power making net electricity more difficult to achieve so that is not examined. Next, the impact of a more peaked density profile is considered. Each of these will indicate their relative

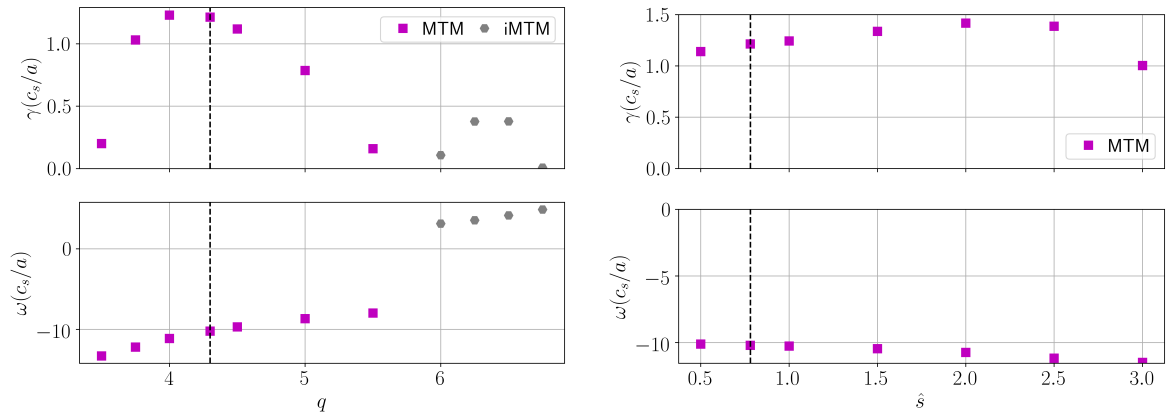

(a) (b)

Figure 20: Impact of a) q and b) $\hat{s}$ on the MTMs at $k_y = 4.2$.

effectiveness at suppressing the KBMs and MTMs.

5.1. Impact of higher toroidal field

It is clear that increasing q destabilises the low k_y MTM. This has some consequences on a higher I_{rod} design which will predominantly change B_φ. At fixed I_p, $\beta_{e,unit} \propto 1/B_\varphi^2$ and $q \propto B_\varphi$, so a high field design may have a lower $\beta_{e,unit}$, stabilising the MTM, but the higher q may act to destabilise it.

To investigate the impact of higher field, SCENE was used to consistently generate equilibria with a higher toroidal field. The value of I_{rod} was increased from $30MA \rightarrow 50MA$, whilst all the other inputs were kept the same. When doing this, most of the equilibrium parameters stayed within 1% of the baseline value. The main parameters that did change for $\rho_\psi = 0.5$ were

- $\beta_{e,unit}$: $0.012 \rightarrow 0.004$
- $\beta'_{e,unit}$: $-0.08 \rightarrow -0.03$
- q : $4.3 \rightarrow 7.3$
- $\hat{s}$: $0.78 \rightarrow 0.70$

Figure 21a illustrates this scan in I_{rod} at $k_y = 0.35$¶, with $\beta_{e,unit}$ shown by the dashed red line. Firstly it is important to note that the KBM and two different MTMs were found in all of these equilibria, suggesting that these will exist over a range of different high β ST equilibria. The KBM is weakly stabilised by the higher rod current. It seems that the stabilisation from the lower $\beta_{e,unit}$ and higher q is counteracted by the lower $\beta'_{e,unit}$. For the MTM there is a very weak stabilisation as the increased q counteracts the lower $\beta_{e,unit}$. If I_{rod} is sufficiently increased, as $\beta_{e,unit} \rightarrow 0$, these modes should become stable, but $I_{rod} = 50MA$ is pushing the limits of engineering so going further beyond this is unlikely to be feasible.

Examining the impact on the high k_y MTM, Figure 21b shows that operating at higher field stabilises the mode and when $I_{rod} > 40MA$, consistent with the $\beta_{e,unit}$, $\beta'_{e,unit}$ scan conducted in Figure 16c. However, the ETG seen there is not destabilised in this scan.

¶ Note this is not at fixed toroidal mode number n as ρ_s changes with B

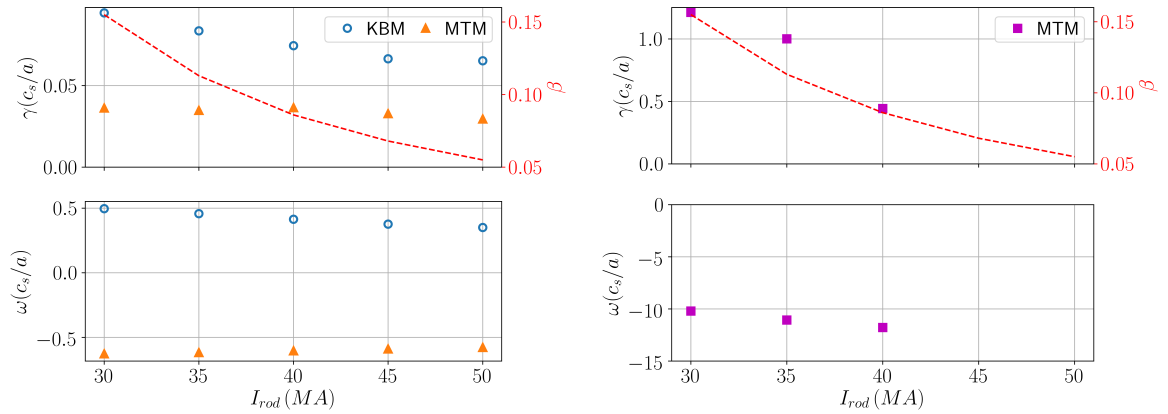

Figure 21: Examining the impact of a higher field device by increasing I_{rod} for a) $k_y = 0.35$ and b) $k_y = 4.2$ at $\rho_\psi = 0.5$.

5.2. Impact of density peaking

The results of the previous sections suggest that the flow shear will wipe out the KBMs and the high k_y MTMs found so far. It was also demonstrated that increasing the density gradient was beneficial in stabilising the low k_y MTMs. If the a/L_T is reduced whilst increasing a/L_n without changing the fusion power, then it may be possible to design an equilibrium in which the majority of the linear instabilities are stable.

Using this information a new equilibrium was designed in SCENE with a more peaked density profile. A scenario was examined where $n_{e0}/\langle n_e \rangle = 1.12$ was increased to $n_{e0}/\langle n_e \rangle = 1.58$ at fixed $P_{fus} = 1.1GW$. The pedestal height and width was kept the same. To reduce the temperature gradient drive for the KBMs, the core temperature for both species was dropped from $28keV$ to $20keV$. The resulting equilibrium parameters are outlined in Table 4.

The parameters are broadly similar to the baseline case, with the exception of the density and temperature values. There is experimental evidence from AUG and JET of achieving $n_{e0}/\langle n_e \rangle \sim 2.0$ with sufficient NBI fuelling [41, 42], which motivates the use of an on axis NBI for heating, current drive and particle deposition, though higher core densities will make penetration more difficult and necessitate high beam energies resulting in low particle deposition. If this is shown not to be sufficient then core pellet injection will need to be examined, though again at such high densities there will be difficulties obtaining sufficient penetration.

The Miller and plasma parameters for the $\rho_\psi = 0.5$ surface is detailed in Table 5. It can be seen that many of the parameters are very similar to the baseline parameters in Table 2, with the notable exception of the higher a/L_n and lower a/L_T as expected. However, a/L_p has increased overall from 6.40 to 7.48, so it may be expected that the KBMs will be driven more unstable, though as seen in earlier sections, this is counteracted by the increased $\beta'_{e,unit}$. $\hat{s}/q$ has increased, due to the differences in the auxiliary, bootstrap and diamagnetic current profiles. This is expected to destabilise the KBMs but its impact on the MTMs is less clear.

The dominant instabilities are presented in Figure 22. Similar to the baseline scenario, in the low k_y region KBMs and extended MTMs are found. However, the peak MTM growth rate is $\gamma_{MTM} = 0.004c_s/a$, significantly lower than the baseline scenario where it was $\gamma_{MTM} = 0.04c_s/a$. The KBM peak growth rate is has increased from $\gamma_{KBM} = 0.09c_s/a$ to $\gamma_{KBM} = 0.19c_s/a$, but these modes are still narrow in θ_0 so it will be shown that again these are wiped out by flow shear. The higher k_y MTMs are also seen and have a lower growth rate reducing from $1.2c_s/a$ to $0.9c_s/a$, and it is expected that the flow shear will help to stabilise these modes as well. Finally above $k_y = 6$, the equilibrium was

Parameter	Value
R_{maj} (m)	2.5
a (m)	1.5
R_0 (m)	3.05
I_{rod} (MA)	30.0
I_p (MA)	21.0
I_{aux} (MA)	7.13
$P_{fus}(MW)$	1100
$P_{aux}(MW)$	83
κ	2.8
δ	0.55
H_{98}, H_{Petty}	1.26, 0.83
$T_{e0}, \langle T_e \rangle (keV)$	22.0, 14.1
$n_{e0}, \langle n_e \rangle (\times 10^{20} m^{-3})$	2.19, 1.38
l_i	0.38
β_N	5.13
q_0	2.07

Table 4: Basic plasma parameters for the optimised scenario

Parameter	$\rho_\psi = 0.5$
r/a	0.67
R_{maj}/a	1.83
n_{e20} (m^{-3})	1.36
$T_e(keV)$	12.8
a/L_n	1.40
a/L_T	2.34
Δ	-0.48
q	3.14
$\hat{s}$	0.97
κ	2.87
s_κ	-0.11
δ	0.34
s_δ	0.21
β_e	0.14
$\beta_{e,unit}$	0.013
ρ^*	0.0014
$\nu_{ei}(c_s/a)$	0.013
$\gamma_{dia}(c_s/a)$	0.055

Table 5: Plasma and Miller parameters for the $\rho_\psi = 0.5$ surface of the optimised equilibrium.

found to be completely stable, similar to the previous case. It should be noted that these modes peak at a lower k_y compared to the baseline case and this is expected as $\rho*$ has not significantly changed but the value of q is lower. Specifically, given that $k_y = nq/r$, to find a given toroidal mode number n at lower q, a lower k_y is needed.

A simulation was run for this case with $E \times B$ flow shear at the diamagnetic level of $\gamma_{dia} = 0.055 c_s/a$. The effective growth rate is shown in Figure 23 and it was found that above $k_y = 0.2$ the equilibrium was completely stable. Below this value, the MTMs did cause a very slowly growing mode with a growth rate $\mathcal{O}(10^{-3})$. The timescale upon which this mode will grow is sufficiently long that the equilibrium will likely evolve before the mode becomes significant. Nonlinear simulations are required to determine the level of driven transport but this work hints that density peaking will be favourable and the plasma may then operate close to neoclassical levels of transport. The impact of impurities and fast ions needs to be examined as they may drive the MTM more unstable, increasing the effective growth rate. In particular, density peaking can lead to impurity accumulation in the core of conventional tokamaks, which would be detrimental to the performance of a reactor. While quantifying the level of impurity accumulation and impact on radiative losses is important, this equilibrium suggests a possible pathway to a high performance high β ST.

The level of density peaking will be set by particle transport and fuelling. The transport for each species can be decomposed into a diffusive term D and a convective term V, shown in Equation 2.

$$\Gamma = D \frac{1}{n} \frac{\partial n}{\partial r} + V \tag{2}$$

The convective particle pinch term from the low k_y MTMs can be examined to determine whether

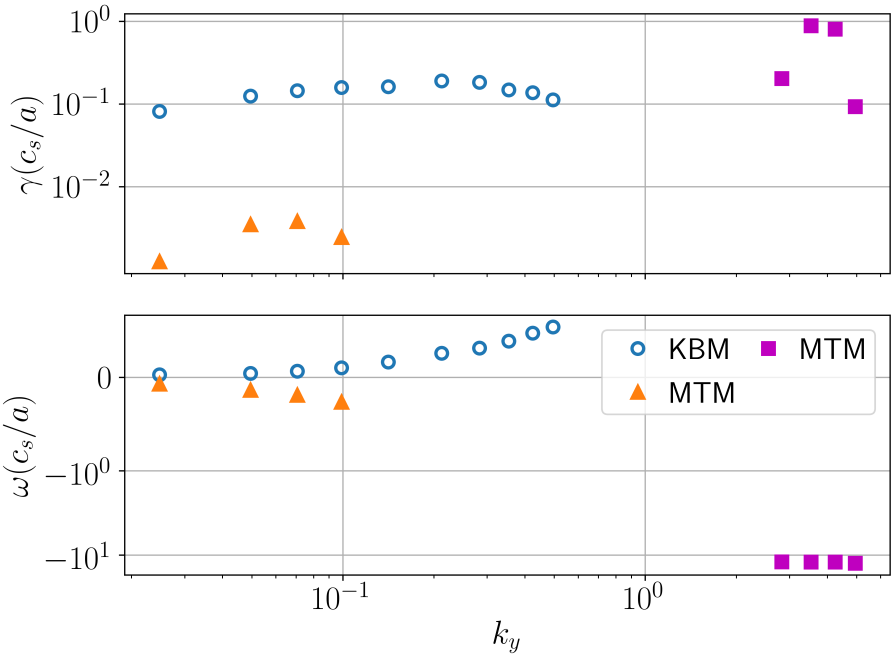

Figure 22: Dominant odd and even mode for the $\rho_\psi = 0.5$ surface of the optimised equilibrium without flow shear outlined in Table 5.

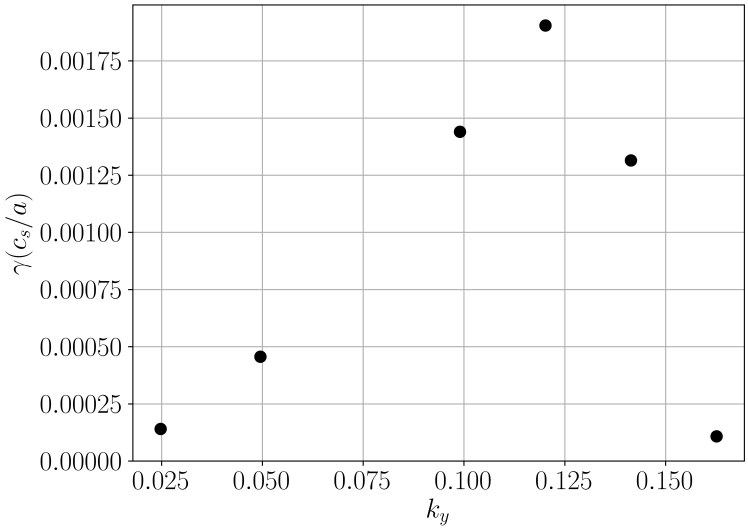

Figure 23: Effective growth rate for the $\rho_\psi = 0.5$ surface of the peaked density equilibrium with diamagnetic levels of flow shear.

it leads to outward or inward particle transport. Using linear physics it is possible to determine the ratio of the convective pinch term V and the diffusivity D shown in Equation 2. By introducing a trace Deuterium species and modifying the trace density gradient finding the point where $\Gamma \to 0$, the ratio of V/D can be determined. Examining $k_y = 0.35$ when $n_{trace,D}/n_e = 0.05$, Figure 24a illustrates that zero particle flux occurs at $a/L_n = -1.56$ meaning $V/D = 1.04m^{-1}$. This means the particle convection is outwards making density peaking even more difficult. The particle flux is normalised to the linear electron heat flux and is $\mathcal{O}(10^{-5})$ so the effect may be small but will not help achieve a peaked density

profile. A similar scan was conducted for the KBMs and they also had an outwards convection, shown in Figure 24b. The relative size of the particle flux is $\mathcal{O}(10^{-2})$, larger than the MTMs but still quite small overall. To achieve peaked density profiles will require further examination if this is to provide a route to a high performance reactor.

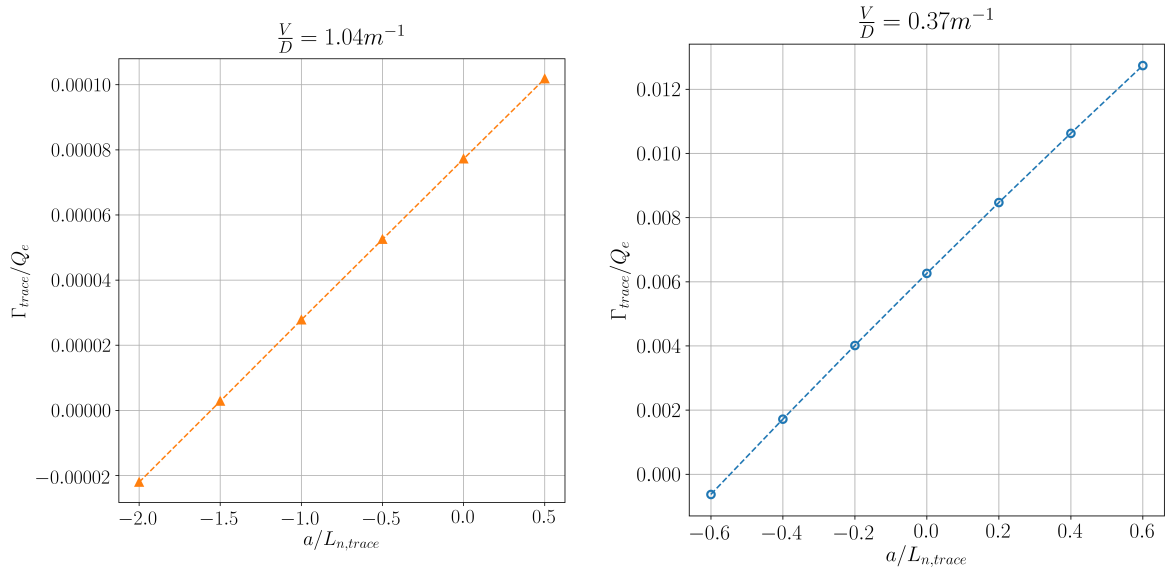

(a) (b)

Figure 24: Linear particle flux of a trace deuterium when scanning through the trace density gradients for the a) MTM and b) KBM at $k_y = 0.35$. The particle flux has been normalised to the electron heat flux.

6. Conclusions

A spherical tokamak with $1GW$ of fusion power was designed and it was found that KBMs and MTMs were the prevalent micro-instabilities in this high β ST equilibrium. Furthermore, the equilibria examined here were found to be stable in the electron scale range where $k_y > 10$.

Two different types of MTMs were found, a collisional MTM when $k_y < 0.6$ and a collisionless MTM between $3.0 < k_y < 6.0$. The KBMs and high k_y MTMs were narrow in θ_0, such that diamagnetic levels of flow shear was sufficient in suppressing these modes. The low k_y MTM, however, was unaffected by flow shear thus is expected to be the dominant source of transport for this equilibrium. These low k_y MTM were very extended in ballooning space suggesting that they require an electron scale radial resolution indicating potential challenge for nonlinear simulations.

The parametric dependency of these modes on different equilibrium parameters was determined and it was found that the low k_y MTMs were primarily stabilised by the density gradient, suggesting that a peaked density profile would be beneficial to confinement. Moreover, the low k_y MTMs were destabilised by ν_*, which is consistent with previous ST experiments, indicating that a high temperature/low density device will benefit the confinement. A complicated dependence on $\beta_{e,unit}$, $\beta'_{e,unit}$ and q led to the interesting result that increasing the toroidal field had little impact on micro-stability of the low k_y modes. Counter-intuitively, this suggests that a higher field device may not improve the confinement.

An optimised equilibrium was generated with a more peaked density profile and flatter temperature profile. With flow shear, the equilibrium was found to be marginally stable, indicating that

operating close to neoclassical levels of transport may be feasible if such an equilibrium can be accessed. The convective pinch term was found to be outwards for both low k_y modes, meaning that achieving density peaking without core fuelling is unlikely. Moreover, the level of impurity accumulation from the density peaking needs to be determined as it may lead to a radiative collapse.

To quantify the level of transport driven from each of these different modes requires nonlinear simulations or a reduced physics model capable of capturing the nonlinear properties of the different types of modes expected to play a role on the transport. This will inform on which modes contribute the most to the transport and thus should be prioritised in their stabilisation.

7. Acknowledgements

The author would like to thank Francis Casson, Walter Guttenfelder, Emily Belli and Jeff Candy for useful discussions that assisted this work.

The views and opinions expressed herein do not necessarily reflect those of the European Commission. This work was supported by the Engineering and Physical Sciences Research Council [EP/L01663X/1, EP/R034737/1, EP/T012250/1]. This work used the ARCHER UK National Supercomputing Service (http://www.archer.ac.uk). We acknowledge the CINECA award under the ISCRA initiative, for the availability of high performance computing resources and support. This research used resources of the National Energy Research Scientific Computing Center (NERSC), a U.S. Department of Energy Office of Science User Facility located at Lawrence Berkeley National Laboratory, operated under Contract No. DE-AC02-05CH11231.

Appendix A. Cross code validation

Given the highly exotic nature of this equilibrium, the predictions made by GS2 were compared to CGYRO to ensure that these modes can be consistently found across codes. CGYRO is currently unable to force and odd or even eigenmode so only the dominant instability can be examined. The results for the $\rho_\psi = 0.5$ surface outlined in Table 2 are shown in Figure A1.

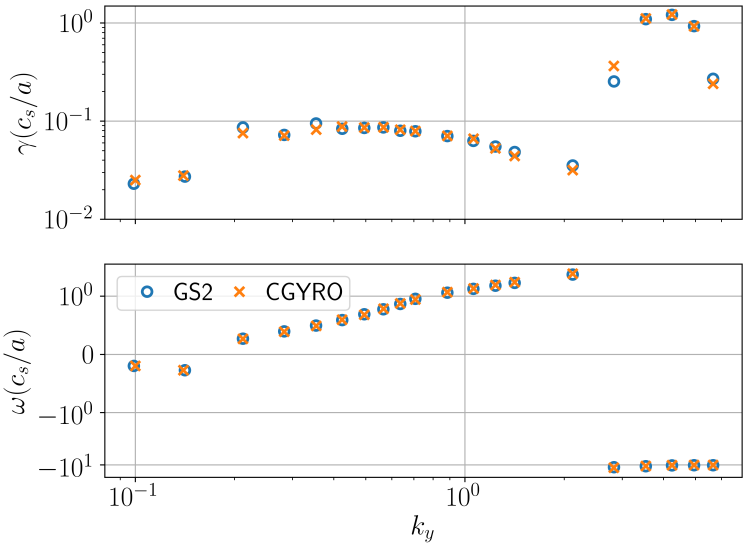

Figure A1: Comparison of the eigenvalue predictions made by GS2 and CGYRO.

It can be seen that both codes are in good agreement for this case, with CGYRO finding these MTMs with the extended mode structure, which indicates that the gyrokinetic equation is being correctly solved and that these modes are likely to appear high β STs like STEP.

Appendix B. Stability of electron scale region

All the equilibria examined so far were found to be stable when $k_y\rho_e \sim \mathcal{O}(1)$. The STPP reactor design was also found to be stable to electron scale modes[43]. ETG-like instabilities are generally found at the electron scale in other tokamaks. To understand why they are stable here, different plasma parameters were scanned as done in the Section 3.2. This section examines the un-optimised case in Table 2 for $\rho_\psi = 0.5$.

Appendix B.1. Impact of kinetic profiles

Given that ETG is expected, the impact of a/L_{Te} was examined. Scans were for $a/L_{Te} = 5.0, 6.0\,\&\,7.0$ for a range of k_y at the electron scale. The equilibrium value of $a/L_{Te} = 2.77$ is well below this temperature gradient range, illustrating the large increase in drive necessary to find any ETG. Figure B1a shows how ETG modes can be found if the drive is sufficiently high. It can be seen that increasing a/L_{Te} does drive the mode seen here unstable, consistent with ETG. This shows that a significant increase in temperature gradient would be necessary for this region of k_y-space to be unstable. The eigenfunction for $k_y = 35$ at $a/L_{Te} = 7.0$ is shown in Figure B1b. The $A_{||}$ component is very small when normalised to ϕ suggesting it is not significant for these ETG modes.

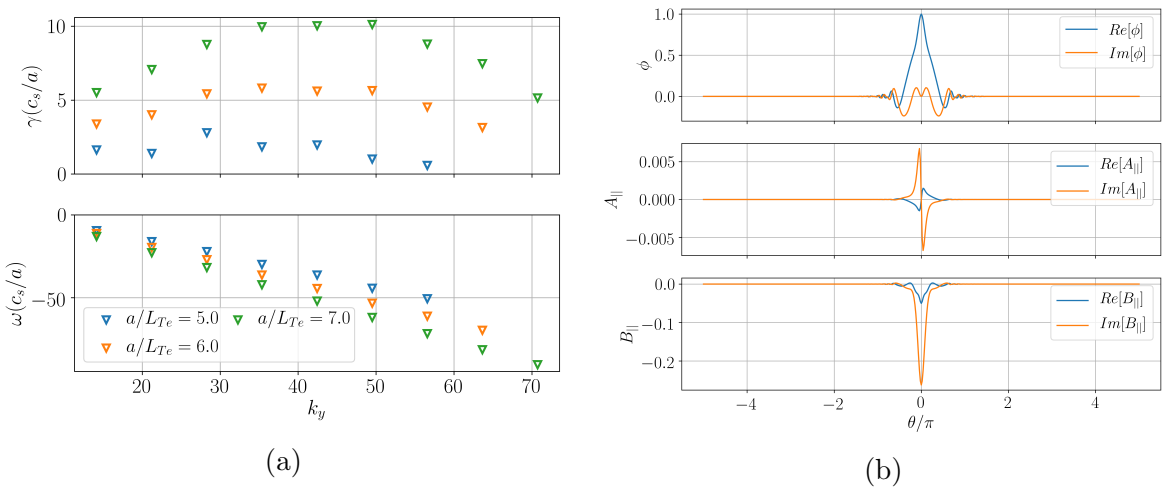

(a) (b)

Figure B1: a) Growth rate spectrum for high values of k_y at different a/L_{Te}. The equilibrium value was $a/L_{Te} = 2.77$. b) Eigenfunctions for $k_y = 35$ when $a/L_{Te} = 7.0$.

To examine why the critical a/L_{Te} is high for this equilibrium other parameters will be examined. The stability at $k_y = 35$ will be investigated more carefully.

Appendix B.2. Impact of magnetic equilibrium

Appendix B.2.1. Impact of $\beta_{e,unit}$ and $\beta'_{e,unit}$ Earlier it was shown that an ETG appeared when reducing $\beta_{e,unit}$ and β'_{unit}. As they were both reduced, the high k_y MTM was stabilised and an ETG was destabilised, so it is expected that they will have an impact on the stability.

Figure B2a shows how the growth rate changes for the 3 different temperature gradients when changing $\beta_{e,unit}$. $\beta_{e,unit}$ is found to be destabilising to these high gradient ETG modes, up to a critical value $\beta_{e,unit} = 0.02$, when there is a rollover and at sufficiently high $\beta_{e,unit}$ these ETG are stabilised. However, at the equilibrium value of a/L_{Te}, the mode was completely stable regardless of the $\beta_{e,unit}$. A similar scan was conducted with $\beta'_{e,unit}$ and this appears to be a cause of the stability. Increasing $\beta'_{e,unit}$ strongly stabilises the ETG mode, such that when $\beta'_{e,unit} = 0$ the ETG mode is unstable even

at the equilibrium a/L_{Te}. This has been seen before by Roach *et al* [44] and is attributed to high β' reducing the bounce average drift frequency, further suggesting the drifts appear to be an important factor in stabilising these ETG modes. This all indicates a potential disadvantage with operating at higher field. The resulting lower $\beta'_{e,unit}$ could destabilise the ETG modes and have a detrimental effect on electron thermal transport.

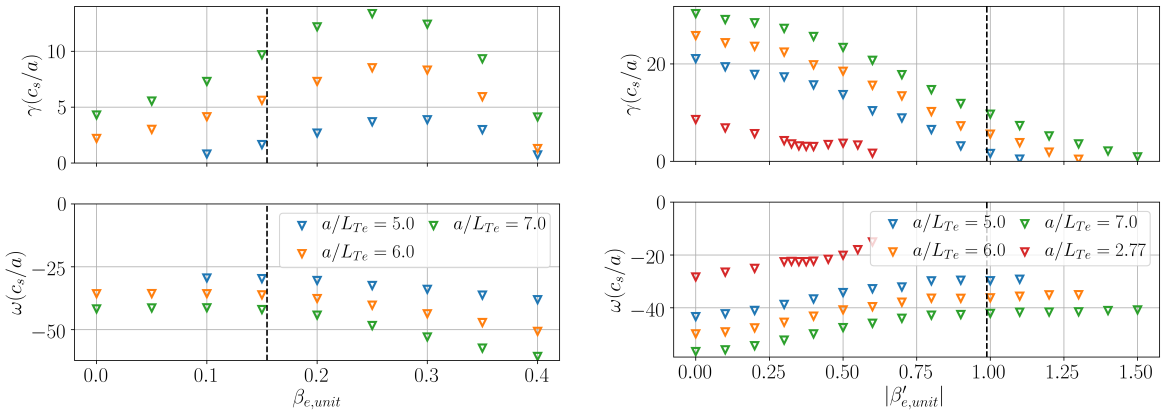

(a) (b)

Figure B2: Impact of a) $\beta_{e,unit}$ and b) $\beta'_{e,unit}$ at different a/L_{Te} with $k_y = 35$.

Appendix B.2.2. Safety factor profile A critical gradient formula for ETG-like turbulence was found by Jenko *et al* [45] as follows

$$\left(\frac{a}{L_{Te}}\right)^{ETG}_{crit} \propto \left(1.3 + 1.9\frac{\hat{s}}{q}\right) \tag{B.1}$$

This was generated from simulations of a low β, conventional aspect ratio tokamak. To examine its validity for this ST equilibrium, scans were performed in a/L_{Te} at different values of q and $\hat{s}$ to find the critical gradient. Equation B.1 suggests that the critical gradient will increase with $\hat{s}/q$ but Figures B3a and B3b indicate this is not the case here. Performing a linear fit to these growth rates, an estimate of the critical gradient can be made and this is shown in Figure B4. It is clear that the scaling of Equation B.1 does not describe this regime. Rather, operating at low $\hat{s}/q$ is actually beneficial to these modes.

This indicates that the scaling laws developed by Jenko are not applicable in this regime such that they cannot be utilised. Though this may not be of a major concern as the ETG was found to be stable for this equilibrium as well as the optimised equilibrium.

Appendix B.3. Higher field device

When examining the impact on the higher gradient cases at $k_y = 35$, Figure B5 shows that operating at higher field does destabilise these ETG modes, indicating the destabilisation from $\beta'_{e,unit}$ is overcoming the stabilisation from lower $\beta_{e,unit}$ and higher q. Nevertheless, for $a/L_{Te} = 2.77$, the modes are stable, so for this case it is not a concern. But it does highlight that operating at higher field may destabilise ETG modes.

References

[1] EDA ITER et al. “Plasma confinement and transport”. In: *Nuclear Fusion* 39.12 ITER physics basis (1999), pp. 2175–2249.

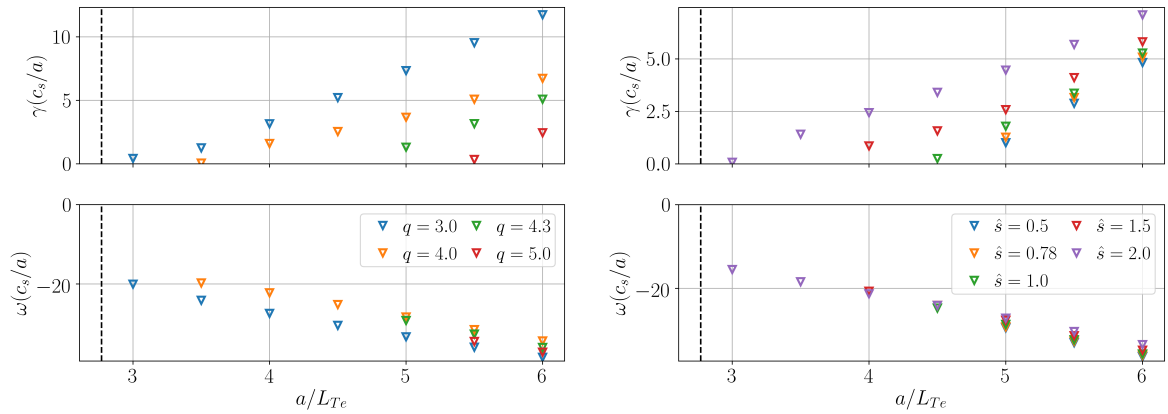

(a) (b)

Figure B3: Impact of a) q and b) $\hat{s}$ with different a/L_{Te} at $k_y = 35$.

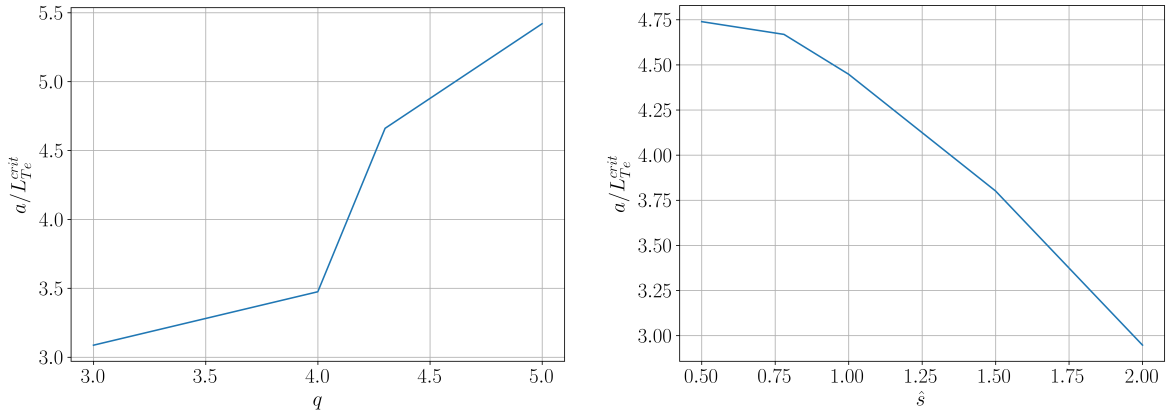

(a) (b)

Figure B4: Critical a/L_{Te} threshold for various a) q and b) $\hat{s}$ at $k_y = 35$.

[2] CC Petty. "Sizing up plasmas using dimensionless parameters". In: *Physics of Plasmas* 15.8 (2008), p. 781.

[3] TL Rhodes et al. "L-mode validation studies of gyrokinetic turbulence simulations via multiscale and multifield turbulence measurements on the DIII-D tokamak". In: *Nuclear Fusion* 51.6 (2011), p. 063022.

[4] F Van Wyk. "Subcritical turbulence in the mega ampere spherical tokamak". In: *arXiv:1703.03397* (2017).

[5] NT Howard et al. "Quantitative comparison of experimental impurity transport with nonlinear gyrokinetic simulation in an Alcator C-Mod L-mode plasma". In: *Nuclear Fusion* 52.6 (2012), p. 063002.

[6] HR Wilson. *SCENE-simulation of self-consistent equilibria with neoclassical effects*. Tech. rep. UKAEA Government Division, 1994.

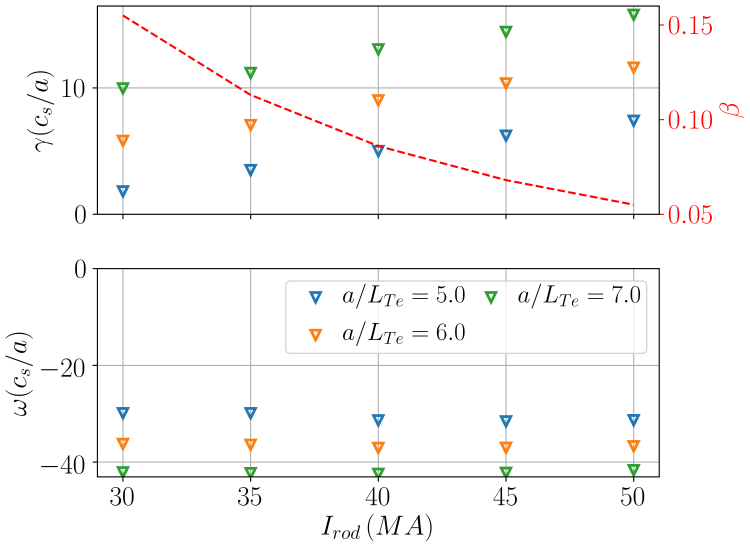

Figure B5: Examining the impact of I_{rod} on the ETG modes for 3 higher temperature gradients at $k_y = 35$. Note the reference equilibrium value is $a/L_{Te} = 2.77$.

[7] JE Menard et al. "Fusion nuclear science facilities and pilot plants based on the spherical tokamak". In: *Nuclear Fusion* 56.10 (2016), p. 106023.

[8] PB Snyder et al. "Pedestal stability comparison and ITER pedestal prediction". In: *Nuclear Fusion* 49.8 (2009), p. 085035.

[9] RJ Akers et al. "Transport and confinement in the Mega Ampere Spherical Tokamak (MAST) plasma". In: *Plasma physics and controlled fusion* 45.12A (2003), A175.

[10] A Pankin et al. "The tokamak Monte Carlo fast ion module NUBEAM in the National Transport Code Collaboration library". In: *Computer Physics Communications* 159.3 (2004), pp. 157–184.

[11] RL Miller et al. "Noncircular, finite aspect ratio, local equilibrium model". In: *Physics of Plasmas* 5.4 (1998), pp. 973–978.

[12] J Candy, EA Belli, and RV Bravenec. "A high-accuracy Eulerian gyrokinetic solver for collisional plasmas". In: *Journal of Computational Physics* 324 (2016), pp. 73–93.

[13] DR Hatch et al. "Microtearing turbulence limiting the JET-ILW pedestal". In: *Nuclear Fusion* 56.10 (2016), p. 104003.

[14] X Jian et al. "Role of Microtearing Turbulence in DIII-D High Bootstrap Current Fraction Plasmas". In: *Physical Review Letters* 123.22 (2019), p. 225002.

[15] D Dickinson et al. "Kinetic instabilities that limit β in the edge of a tokamak plasma: a picture of an H-mode pedestal". In: *Physical Review Letters* 108.13 (2012), p. 135002.

[16] W Guttenfelder et al. "Progress in simulating turbulent electron thermal transport in NSTX". In: *Nuclear Fusion* 53.9 (2013), p. 093022.

[17] N Kumar et al. "Turbulent transport driven by kinetic ballooning modes in the inner core of JET hybrid H-modes". In: *Nuclear Fusion* (2020).

[18] D Dickinson et al. "Towards the construction of a model to describe the inter-ELM evolution of the pedestal on MAST". In: *Plasma physics and controlled fusion* 53.11 (2011), p. 115010.

[19] DR Hatch. *Mode analyses of gyrokinetic simulations of plasma microturbulence*. 2010.

[20] A Ishizawa et al. "Electromagnetic gyrokinetic simulation of turbulence in torus plasmas". In: *Journal of Plasma Physics* 81.2 (2015).

[21] CM Roach et al. "Confinement in START beam heated discharges". In: *Nuclear fusion* 41.1 (2001), p. 11.

[22] W Guttenfelder et al. "Electromagnetic transport from microtearing mode turbulence". In: *Physical review letters* 106.15 (2011), p. 155004.

[23] JF Drake and YC Lee. "Kinetic theory of tearing instabilities". In: *The Physics of Fluids* 20.8 (1977), pp. 1341–1353.

[24] T Rafiq et al. "Microtearing modes in tokamak discharges". In: *Physics of Plasmas* 23.6 (2016), p. 062507.

[25] DJ Applegate et al. "Microstability in a "MAST-like" high confinement mode spherical tokamak equilibrium". In: *Physics of plasmas* 11.11 (2004), pp. 5085–5094.

[26] W Guttenfelder et al. "Scaling of linear microtearing stability for a high collisionality National Spherical Torus Experiment discharge". In: *Physics of Plasmas* 19.2 (2012), p. 022506.

[27] AB Hassam. "Fluid theory of tearing instabilities". In: *The Physics of Fluids* 23.12 (1980), pp. 2493–2497.

[28] PJ Catto and MN Rosenbluth. "Trapped electron modifications to tearing modes in the low collision frequency limit". In: *The Physics of Fluids* 24.2 (1981), pp. 243–255.

[29] DJ Applegate et al. "Micro-tearing modes in the mega ampere spherical tokamak". In: *Plasma Physics and Controlled Fusion* 49.8 (2007), p. 1113.

[30] AK Swamy et al. "Collisionless microtearing modes in hot tokamaks: Effect of trapped electrons". In: *Physics of Plasmas* 22.7 (2015), p. 072512.

[31] D Dickinson et al. "Microtearing modes at the top of the pedestal". In: *Plasma Physics and Controlled Fusion* 55.7 (2013), p. 074006.

[32] Chen Geng, David Dickinson, and Howard Wilson. "The physics of a small-scale tearing mode in collisionless slab plasmas". In: *Plasma Physics and Controlled Fusion* 62.8 (2020), p. 085009.

[33] EA Belli and J Candy. "Fully electromagnetic gyrokinetic eigenmode analysis of high-beta shaped plasmas". In: *Physics of Plasmas* 17.11 (2010), p. 112314.

[34] DR Hatch et al. "A gyrokinetic perspective on the JET-ILW pedestal". In: *Nuclear Fusion* 57.3 (2017), p. 036020.

[35] EG Highcock. "The zero turbulence manifold in fusion plasmas". In: *arXiv preprint arXiv:1207.4419* (2012).

[36] HS Xie, ZX Lu, and B Li. "Kinetic ballooning mode under steep gradient: High order eigenstates and mode structure parity transition". In: *Physics of Plasmas* 25.7 (2018), p. 072106.

[37] M Valovič et al. "Collisionality and safety factor scalings of H-mode energy transport in the MAST spherical tokamak". In: *Nuclear Fusion* 51.7 (2011), p. 073045.

[38] I Predebon and F Sattin. "On the linear stability of collisionless microtearing modes". In: *Physics of Plasmas* 20.4 (2013), p. 040701.

[39] RJ Groebner et al. "Limits to the H-mode pedestal pressure gradient in DIII-D". In: *Nuclear fusion* 50.6 (2010), p. 064002.

[40] JW Connor, RJ Hastie, and John Bryan Taylor. "High mode number stability of an axisymmetric toroidal plasma". In: *Proceedings of the Royal Society of London. A. Mathematical and Physical Sciences* 365.1720 (1979), pp. 1–17.

[41] ASDEX Upgrade Team et al. "Density peaking, anomalous pinch, and collisionality in tokamak plasmas". In: *Physical review letters* 90.20 (2003), p. 205003.

[42] C Angioni et al. "Scaling of density peaking in H-mode plasmas based on a combined database of AUG and JET observations". In: *Nuclear fusion* 47.9 (2007), p. 1326.

[43] HR Wilson et al. "Integrated plasma physics modelling for the Culham steady state spherical tokamak fusion power plant". In: *Nuclear fusion* 44.8 (2004), p. 917.

[44] CM Roach, JW Connor, and S Janjua. "Trapped particle precession in advanced tokamaks". In: *Plasma physics and controlled fusion* 37.6 (1995), p. 679.

[45] F Jenko, W Dorland, and GW Hammett. "Critical gradient formula for toroidal electron temperature gradient modes". In: *Physics of Plasmas* 8.9 (2001), pp. 4096–4104.